

# The role of grain dynamics in determining the onset of sediment transport

Abram H. Clark,<sup>1</sup> Mark D. Shattuck,<sup>2</sup> Nicholas T. Ouellette,<sup>3</sup> and Corey S. O'Hern<sup>1,4,5</sup>

<sup>1</sup>*Department of Mechanical Engineering and Materials Science,  
Yale University, New Haven, Connecticut 06520, USA*

<sup>2</sup>*Benjamin Levich Institute and Physics Department,  
The City College of the City University of New York, New York, New York 10031, USA*

<sup>3</sup>*Department of Civil and Environmental Engineering,  
Stanford University, Stanford, California 94305, USA*

<sup>4</sup>*Department of Physics, Yale University, New Haven, Connecticut 06520, USA*

<sup>5</sup>*Department of Applied Physics, Yale University, New Haven, Connecticut 06520, USA*

Sediment transport occurs when the nondimensional fluid shear stress  $\Theta$  at the bed surface exceeds a minimum value  $\Theta_c$ . A large collection of data, known as the Shields curve, shows that  $\Theta_c$  is primarily a function of the shear Reynolds number  $Re_*$ . It is commonly assumed that  $\Theta > \Theta_c(Re_*)$  occurs when the  $Re_*$ -dependent fluid forces are too large to maintain static equilibrium for a typical surface grain. A complimentary approach, which remains relatively unexplored, is to identify  $\Theta_c(Re_*)$  as the applied shear stress at which grains cannot stop moving. With respect to grain dynamics,  $Re_*$  can be viewed as the viscous time scale for a grain to equilibrate to the fluid flow divided by the typical time for the fluid force to accelerate a grain over the characteristic bed roughness. We performed simulations of granular beds sheared by a model fluid, varying only these two time scales. We find that the critical Shields number  $\Theta_c(Re_*)$  obtained from the model mimics the Shields curve and is insensitive to the grain properties, the model fluid flow, and the form of the drag law. Quantitative discrepancies between the model results and the Shields curve are consistent with previous calculations of lift forces at varying  $Re_*$ . Grains at low  $Re_*$  find more stable configurations than those at high  $Re_*$  due to differences in the grain reorganization dynamics. Thus, instead of focusing on mechanical equilibrium of a typical grain at the bed surface,  $\Theta_c(Re_*)$  may be better described by the stress at which mobile grains cannot find a stable configuration and stop moving.

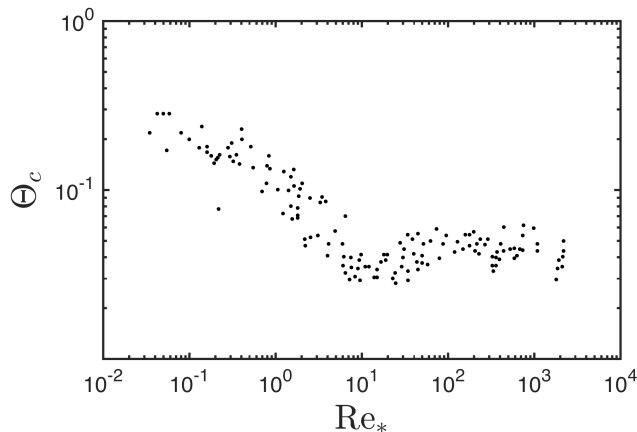


FIG. 1. A collection of experimental and field data from Dey [4] showing the variation of the minimum Shields number for grain motion  $\Theta_c$  with the shear Reynolds number  $Re_*$ .

## I. INTRODUCTION

A fluid that flows over a granular bed exerts a shear stress on the grains and, if the flow is sufficiently strong, will entrain grains in the flow. This process is responsible for shaping much of the natural world. Understanding and controlling the erosion of sediments by flowing water are significant for a range of ecological and agricultural problems [1–3]. Thus, the nature of the onset and cessation of grain motion in the presence of a fluid shear flow has been the subject of extensive research dating back many decades (for example, see recent reviews by Dey [4] and Buffington and Montgomery [5]), but it is still not fully understood. This problem involves nontrivial coupling between several physical processes that are each difficult to characterize. Predicting the dynamics of granular materials is challenging, even for very simple cases like frictionless disks [6]. In the natural world, the geological processes that produce the granular materials in question yield grains with varying size, shape, roughness, and other material properties [7]. The mechanics of the flow that imparts stress to the bed are also nontrivial, given both the wide range of channel geometries in natural streams and rivers [8, 9] and possibly turbulent conditions. Additionally, the fluid inside the bed is also moving, as the bed can be viewed as a porous material, and is governed by Darcy flow [10], although with a complicated boundary condition linking it to the turbulent flow at the bed surface.

Despite the apparent complexity of this problem, there is evidence that the boundary in parameter space between mobile and static beds can be described relatively simply. In particular, a collection of data dating back over a century, shown in Fig. 1, suggests that the onset of grain motion can be captured by only two nondimensional parameters [4, 5, 11–23]. First, the Shields number  $\Theta = \frac{\tau}{\Delta\rho g D}$  compares the horizontal shear stress  $\tau$  exerted by the fluid at the bed surface to the downward gravitational stress  $\Delta\rho g D$ , where  $\Delta\rho = \rho_g - \rho_f$ ,  $\rho_g$  and  $\rho_f$  are the mass densities of the grains and fluid,  $g$  is the gravitational acceleration, and  $D$  is the typical grain diameter. The minimum Shields number  $\Theta_c$  required for grain motion is plotted as a function of the shear Reynolds number  $Re_* = u_* D / \nu$ , where  $u_*^2 = \tau / \rho_f$  and  $\nu$  is the kinematic viscosity of the fluid. Figure 1 shows data for  $\Theta = \Theta_c$  versus  $Re_*$  taken from Dey [4], who compiled data from a range of sources [11–23]. These data, often referred to as the Shields curve, were collected over a wide range of different flows, spanning the range from laminar to fully turbulent, and for many channel geometries and grain properties. Although the data are scattered, they cluster around a master curve. However, why the Shields curve takes this particular form and why that form is so robust against variation of other parameters remain open questions.

### A. Prior descriptions of the Shields curve

There have been a number of approaches aimed at explaining the shape of the Shields curve. (See Dey [4] for a comprehensive treatment.) To date, the most successful descriptions are hydraulic or empirical scaling formulas [13, 22–26]; see Paphitis [27] for a review of these models. This approach was pioneered by Shields [13], who originally found that  $\Theta_c$  varies with  $Re_*$ . To explain the data collapse, he noted that  $Re_*$  controls the ratio of the boundary roughness (set by the grain size  $D$ ) to the size of the viscous sublayer. The Shields curve can then be broken into regions where grains are, as compared to the viscous sublayer, completely submerged ( $Re_* < 2$ ), near the top ( $2 < Re_* < 10$ ),

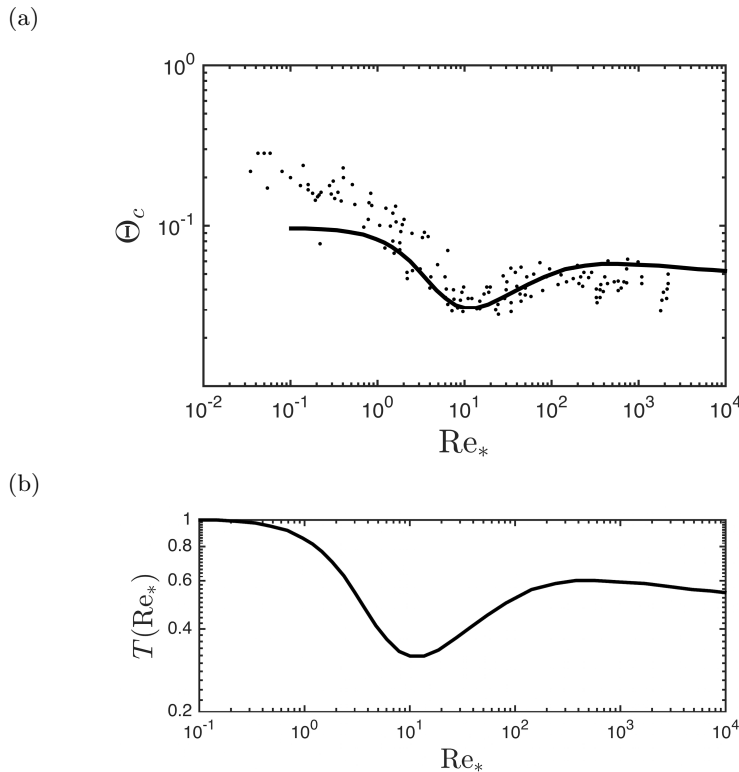


FIG. 2. (a) The same data from Fig. 1, shown with the theoretical curve (solid black line) for monodisperse sediment derived by Wiberg and Smith [29]; see text for discussion. (b) The curve  $T(Re_*, \Theta_c, \phi)$  which accounts for lift forces at varying  $Re_*$ . This curve is calculated by dividing the solid black curve shown in panel (a) by  $\Theta_{c,0} \approx 0.1$ , which is determined by the pocket geometry. (See Fig. 3.) Wiberg and Smith [29] showed that, for monodisperse sediment, the magnitude  $\Theta_{c,0}$  depends strongly on the pocket geometry, but the curve  $T(Re_*)$  remains approximately the same for monodisperse sediment.

partially protruding ( $10 < Re_* < 1000$ ), and fully protruding ( $Re_* > 1000$ ). These regions appear to coincide with distinct regimes on the Shields curve. Others have tried a similar approach, where  $\Theta_c$  is plotted as a function of different nondimensional parameters. For instance, the Yalin number  $\Xi = Re_*/\sqrt{\Theta_c}$  [25] and dimensionless grain diameter  $D_*$  [26] have been used to eliminate the shear stress dependence on the horizontal axis. These approaches have the advantages of being based in grain scale fluid mechanics and being highly predictive, but they still require an empirical fit to the data shown in Fig. 1.

Attempts at a more theoretical derivation [28–32] of the shape of the Shields curve are typically based on static force and torque balance of a typical grain that resides on the surface of the bed. Thus, the variation of  $\Theta_c$  with  $Re_*$  is assumed to be a purely fluid-driven effect. The Shields curve denotes the maximum stress at which a grain on the bed surface in a typical geometric configuration remains in static equilibrium given the  $Re_*$ -dependent contributions from lift, drag, and turbulence. However, since these calculations consider a single grain in a particular local environment, they are highly sensitive to the local grain environment. The local grain environment is often called a “pocket” with pocket angles  $\phi$  that specify the orientation of grain-grain contacts [33–36].

A notable example of this approach by Wiberg and Smith [29] considered a quasi-two-dimensional case where a grain sits in a pocket and motion is initiated when the downstream forces exceed the resistive forces. The only inputs to the calculation are the pocket angle  $\phi$  and the form of the fluid flow at varying  $Re_*$ : a logarithmic form for  $Re_* > 100$  and a form proposed by Reichardt [37] for  $Re_* < 100$  that has been shown to agree well with experiments [38]. Wiberg and Smith [29] then directly calculated the drag and lift forces from the appropriate fluid profiles at different values of  $Re_*$ . Small grains ( $Re_* \ll 1$ ) are buried deep in the viscous sublayer, and lift forces are small. As  $Re_*$  increases, grains begin to protrude out of the viscous sublayer, and lift forces increase rapidly compared to drag forces. This regime corresponds to the global minimum in the Shields curve at  $Re_* \approx 10$ . Large grains ( $Re_* \gg 10$ ) protrude far into the overlying logarithmic flow profile. In this case, lift forces persist, but their effect becomes less pronounced relative to the drag force.

From this calculation,  $\Theta_c$  can be written in terms of  $\phi$  and  $Re_*$  as

$$\Theta_c = \Theta_{c,0}(\phi)T(Re_*, \Theta_c, \phi). \quad (1)$$

The magnitude  $\Theta_{c,0}$  at  $\text{Re}_* \ll 1$ , where lift forces are relatively small, is determined by  $\phi$ . This value is modulated by a function  $T(\text{Re}_*, \Theta_c, \phi)$  that accounts for the lift forces at a given  $\text{Re}_*$ ,  $\Theta_c$ , and  $\phi$ . That is, by accounting for lift forces,  $\Theta$  is converted to an effective Shields number  $\Theta_{c,0}$ , which represents the ratio of total downstream stresses to vertical stresses (gravity minus lift) required to move the grain out of its pocket. The result of this calculation for monodisperse sediment is shown in Fig. 2, where the bed roughness  $k_s$  is equivalent to the grain size  $D$ .

This curve captures the global minimum in the Shields curve at  $\text{Re}_* \approx 10$ , corresponding to conditions where the grain size is roughly equal to the size of the viscous sublayer. While  $\Theta_{c,0}$  varies with  $\phi$ ,  $T(\text{Re}_*, \Theta_c, \phi)$  depends only weakly on  $\phi$  and  $\Theta_{c,0}$ ; see Fig. 3(a) in Wiberg and Smith [29].  $\Theta_{c,0}$  is essentially a fit parameter, and it is very sensitive to the local grain geometry. The critical Shields curve for  $\Theta_{c,0} \approx 0.1$  is shown in Fig. 2(a). This curve agrees well with data for  $\text{Re}_* > 1$ , but it underestimates  $\Theta_c$  at low  $\text{Re}_*$ .  $\Theta_{c,0}$  between 0.2 and 0.3 would better capture the data at low  $\text{Re}_*$ . However,  $\Theta_{c,0}$  is purely a function of grain geometry, and when using this approach there is no clear physical reason to choose a larger  $\Theta_{c,0}$  for small  $\text{Re}_*$ . These approaches based on static force and torque balance have been successful at capturing certain features of the Shields curve, but not the quantitative shape over the full range of  $\text{Re}_*$ . For a more thorough review of similar approaches, see [4].

## B. The role of grain dynamics

However, a theoretical description for  $\Theta_c(\text{Re}_*)$  that includes  $\text{Re}_*$ -dependent grain dynamics may be combined with such approaches to explain how beds could be stronger at low  $\text{Re}_*$ . For example, grain motion can be temporary, as individual grains that are unstable at a particular shear force can find more stable locations. Depending on the preparation history of the bed, grains may move initially when a shear flow is applied, but the bed may grow stronger as grains search and find more stable configurations [33, 39–41]. That is, mobilized grains can often find a more stable pocket than the original one and stop moving, and this effect is usually neglected in theoretical considerations. How does  $\text{Re}_*$  affect the dynamics of grains as they search for stability? How do the results of such a collective search compare to the Shields curve? This manuscript will address these two important questions.

To this end, we note that in addition to comparing the grain size to the viscous sublayer size,  $\text{Re}_*$  is the ratio of two time scales related to grain motion. The characteristic viscous time for a single grain to equilibrate to the fluid flow is given by  $\tau_\nu = \frac{\rho_g D^2}{\rho_f \nu}$ . Since  $\Theta$  is the ratio of horizontal to vertical stresses, the characteristic horizontal acceleration of a grain is given by  $\Theta g'$ , and thus, under constant acceleration conditions, the characteristic time for the boundary shear stress to accelerate a grain over a distance  $D$  is given by  $\tau_\Theta = \sqrt{\frac{D}{\Theta g'}}$ , where  $g' = \left(\frac{\rho_g - \rho_f}{\rho_g}\right) g$  is the buoyancy-corrected gravitational acceleration experienced by a grain. It is easily shown that  $\text{Re}_* = \sqrt{\frac{\rho_f}{\rho_g}}(\tau_\nu / \tau_\Theta)$ . Thus, when  $\text{Re}_* \ll 1$ ,  $\tau_\nu \ll \tau_\Theta$ , and grains quickly equilibrate to the local fluid velocity. When  $\text{Re}_* \gg 1$ ,  $\tau_\nu \gg \tau_\Theta$ , and mobile grains near the surface undergo collisions with other grains on the bed surface before they equilibrate to the local fluid speed. (See Sec. II for a more detailed discussion.)

To test this interpretation, we present the results of discrete-element method (DEM) simulations, where we allow a bed of grains to search for stable configurations under an applied fluid-like shear force. We prepare ensembles of mobilized beds, and we vary the magnitude of the applied fluid velocity to determine the critical shear force at which grain motion is sustained indefinitely. For simulations where grains stop moving, we increase the magnitude of the shear force to determine the critical shear force at which sustained grain motion is initiated. While many DEM-based approaches include as much physical realism as possible [42–46], we here simplify the problem to isolate the role of  $\text{Re}_*$  as the ratio of the two time scales controlling grain dynamics. Grains are driven by a model fluid shear flow that is small in densely packed regions (i.e., in the interior of the bed) and large in sparsely packed regions (i.e., above the bed). Thus, the force on a static bed is applied almost exclusively to the top layer, and grains that protrude farther out of the bed experience stronger forces. The model fluid flow, which does not vary with  $\text{Re}_*$ , is then coupled to the velocity of the grains through a drag law, which sets  $\text{Re}_*$ . In contrast to recent work with a linear drag law and frictionless, elastic disks [47], here we show results from simulations with complex grain properties and a more realistic fluid drag law. Specifically, we study both two-dimensional (2D) and three-dimensional (3D) systems with friction (in 2D only), irregular grain shape (in 2D only), and significant grain-grain dissipation (both in 2D and 3D) using linear and quadratic drag laws (3D only).

In both 2D and 3D systems, we find a single boundary  $\Theta_c(\text{Re}_*)$  separating mobile and static systems. Mobile grains will stop for  $\Theta < \Theta_c$ , and sustained grain motion will occur for  $\Theta > \Theta_c$ .  $\Theta_c(\text{Re}_*)$  from simulations consists of plateaus  $\Theta_c(\text{Re}_* < 1) = \Theta_c^l$  and  $\Theta_c(\text{Re}_* > 10) = \Theta_c^h$ , with a crossover from  $1 < \text{Re}_* < 10$  that connects the two plateau regions. In 3D,  $\Theta_c^l \approx 0.28$  and  $\Theta_c^h \approx 0.11$ .  $\Theta_c^l \approx 0.28$  agrees quantitatively with the data in Fig. 1. These results suggest that there may indeed be a plateau in the Shields curve for  $\Theta_c(\text{Re}_* \ll 1)$  [48]. In contrast,  $\Theta_c^h \approx 0.11$  is larger than the data for the Shields curve by roughly a factor 2, but this is consistent with the relative contribution

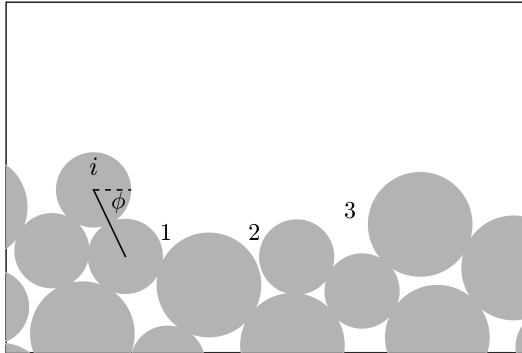


FIG. 3. Grain  $i$  will move when the ratio of horizontal (rightward) to vertical (downward) forces is equal to  $\cot \phi$ . Possible landing sites (pockets) are marked 1, 2, and 3. As we discuss in the text, whether the grain will stop after motion is initiated depends both on the geometrical details of the pockets as well as the dynamics of the grain motion, which vary with  $\text{Re}_*$ .

of lift forces in this regime [29] and possibly a contribution from turbulent fluctuations [49–52]. We also find that  $\Theta_c(\text{Re}_*)$  in simulations is highly insensitive to the details of the fluid flow, grain properties, and the form of the drag law used. The last point is interesting, since it is often assumed [13] that the functional form of the fluid force acting on the grains is responsible for the plateau at  $\text{Re}_* \gg 1$ , where inertial forces become dominant.

Our results suggest that  $\text{Re}_*$ -dependent grain dynamics play a key role in setting the shape of the Shields curve. We argue that instead of focusing on static force and torque balance on typical grains, the onset of bedload transport might be better understood as a collective granular dynamics problem, where mobilized grains search for stability at different  $\text{Re}_*$ . At low  $\text{Re}_*$ , the threshold for sustained grain motion is determined by the most stable condition of the top layer of grains in a disordered bed, as grains perform a search for stable configurations in the absence of inertia. The threshold for sustained grain motion at high  $\text{Re}_*$  is determined by the dynamics of grains that are accelerated significantly between successive interactions with the bed. Essentially, grains can find states that are geometrically stronger at low  $\text{Re}_*$ , and these states become inaccessible at high  $\text{Re}_*$  due to the difference in the grain dynamics, which vary from viscous-dominated at low  $\text{Re}_*$  to acceleration-dominated at high  $\text{Re}_*$ .

We organize the remainder of the manuscript as follows. Section II gives a discussion of the grain dynamics along with relevant dimensional analysis. Section III discusses the numerical methods used to carry out the simulations. Section IV describes our main results, followed by more detailed analysis. Section IV A compares results in 3D using linear and quadratic drag laws. Section IV B shows results in 2D, where  $\Theta_c(\text{Re}_*)$  increases by roughly a factor of two compared to that in 3D, which we attribute to the surface geometry in 2D versus 3D beds. We use 2D simulations to show that  $\Theta_c(\text{Re}_*)$ , from the perspective of grain dynamics, is insensitive to grain properties and the details of the fluid flow. Section IV C shows that grain motion is always initiated at the dynamical boundary  $\Theta_c(\text{Re}_*)$ , with a system size dependence that is well described by weakest-link statistics. Finally, Section V contains a summary of the main points and conclusions from our work.

## II. $\text{Re}_*$ CONTROLS GRAIN DYNAMICS

To illustrate the effects of  $\text{Re}_*$ -dependent grain dynamics, we first consider a simple example of a grain sitting on top of a 2D bed, shown in Fig. 3. Grain  $i$  will become unstable when the ratio of the horizontal fluid force (rightward) and vertical forces (gravity minus lift forces) is  $\cot \phi$ . After this grain becomes unstable (i.e., not in force and torque balance) at the surface of the bed, the subsequent dynamics depend strongly on  $\text{Re}_*$ . The mobilized grain can then land and remain in one of the other pockets on the bed surface, labeled 1-3, depending on geometry, grain properties, and the amount of momentum it has acquired. That is, for the grain to land in one of the pockets, the grain must be stable in that pocket at the given  $\Theta$  and it must be moving sufficiently slowly to stop in the pocket. The amount of momentum acquired can be approximated by the product of the force experienced by the grain at rest times the characteristic time scale over which that force was able to act. For  $\text{Re}_* \ll 1$ , this time scale is very short, since viscous effects cause the grain to equilibrate to the fluid flow almost immediately. For  $\text{Re}_* \gg 1$ , all relevant fluid equilibration time scales are longer than the time between interactions with the bed, and the grain will feel nearly constant acceleration between successive collisions with the bed.

If we approximate the motion of a mobile grain as that of a sphere in a uniform fluid flow, then the drag force is given by  $F_D = 1/2 C_d \rho_f A_x V^2$ , where  $A_x = \frac{\pi}{4} D^2$  is the cross sectional area of the sphere, the drag coefficient  $C_d \approx \frac{24}{\text{Re}_p} + 0.4$ , the particle Reynolds number  $\text{Re}_p = VD/\nu$ , and  $V$  is the slip velocity between the fluid and the sphere. The first term,  $24/\text{Re}_p$ , in  $C_d$  captures Stokes drag (linear in  $V$ ) and the second term, 0.4, captures inertial drag (quadratic in  $V$ ). The dynamics can thus be written as

$$\left(\rho_g \frac{\pi}{6} D^3\right) \frac{dV}{dt} = -(3\pi\rho_f\nu D)V - \left(\frac{\pi}{20}\rho_f D^2\right) V^2, \quad (2)$$

where  $\rho_g \frac{\pi}{6} D^3$  is the grain mass. The solution to this equation is

$$V(t) = V_0 \frac{\exp(-t/\tau_\nu)}{1 + \frac{\text{Re}_p^0}{60} [1 - \exp(-t/\tau_\nu)]}, \quad (3)$$

where  $\tau_\nu \propto \frac{\rho_g D^2}{\rho_f \nu}$  is the viscous equilibration time scale,  $\text{Re}_p^0 = V_0 D/\nu$  is the initial particle Reynolds number, and  $V_0$  is the slip velocity at  $t = 0$ . If  $\text{Re}_p^0 \ll 1$ , then  $V(t) = V_0 \exp(-t/\tau_\nu)$ , and the viscous time scale specifies the dynamics. If  $\text{Re}_p^0 \gg 1$ , then  $\tau_\nu$  becomes large, and a Taylor expansion of the exponential terms in Eq. (3) yields  $V(t) = V_0 \left(1 + \frac{t}{\tau_I}\right)^{-1}$ , where  $\tau_I \propto \frac{\rho_g D}{\rho_f V_0}$ . (This solution is also obtained by integrating Eq. (2) with the Stokes drag term set to zero.) We note that even for  $\text{Re}_p^0 \gg 1$ ,  $\tau_\nu$  still dominates the final portion of the dynamics.

Assuming a constant acceleration  $\Theta g'$ , the dimensionless shear stress  $\Theta$  takes a characteristic time  $\tau_\Theta \propto \sqrt{\frac{D}{\Theta g'}}$  to accelerate a grain through a distance  $D$ , which is the typical spacing between successive collisions with the bed. Here,  $g'$  is the buoyancy-reduced gravitational acceleration, so  $\Theta g'$  is the typical acceleration that a grain first experiences after it becomes unstable. (We note that  $\tau_\Theta$  can also be written as  $\tau_\Theta \propto \sqrt{\frac{\rho_g}{\rho_f} \frac{D}{u_*}}$ . The form we have chosen emphasizes its connection to horizontal acceleration of grains along the bed surface.) However, the acceleration of a mobile grain will eventually be cut off by equilibrating to the fluid flow. Thus, the bed collision time scale  $\tau_\Theta$  should be compared to the fluid equilibration time scales  $\tau_\nu$  and  $\tau_I$ . It can be shown that  $\text{Re}_*$  compares the viscous equilibration time scale to the bed collision time scale,

$$\text{Re}_* = \sqrt{\frac{\rho_f}{\rho_g} \frac{\tau_\nu}{\tau_\Theta}}. \quad (4)$$

For  $\text{Re}_* \ll 1$ , a mobilized grain quickly equilibrates to the fluid flow. Thus, it is not significantly accelerated between interactions with the bed, it acquires very little momentum, and its dynamics are viscous-dominated. In this case, the effect of grains bouncing over geometrically stable pockets should be negligible. If the grain finds a geometrically stable location, it will stop. When  $\text{Re}_* \gg 1$ , a mobilized grain is accelerated between successive interactions with the bed, acquiring momentum  $p \sim \Theta m g' \tau_\Theta$ , and its dynamics are acceleration-dominated. For  $\text{Re}_* \gg 1$ , the inertial time scale is dominant, meaning that  $\tau_I/\tau_\Theta$  is the relevant ratio, instead of  $\tau_\nu/\tau_\Theta$ . This ratio is a constant,  $\tau_I/\tau_\Theta = \sqrt{\rho_g/\rho_f}$ . Physically, this means that further increasing  $\text{Re}_*$  does not cause the grains to be accelerated for longer times. However, a typical ratio  $\rho_g/\rho_f \approx 3$  for rocks, minerals, and soils still yields  $\tau_I > \tau_\Theta$ . This means that, for  $\text{Re}_* \gg 1$ , weakly mobilized grains will still interact with the bed before fully equilibrating to the fluid flow [52, 53]. Thus, for larger values of  $\text{Re}_*$ , the grain is accelerated, and the grain's momentum could either carry it over a stable pocket, or it could reshape the pocket by dislodging other grains in its interaction with the bed. This framework provides a mechanism whereby grains can find stable geometrical configurations at low  $\text{Re}_*$  that become inaccessible at high  $\text{Re}_*$ .

### III. METHODS

#### A. Equations of motion and grain-grain interactions

We study systems composed of  $N/2$  large and  $N/2$  small grains with diameter ratio 1.4 in 2D [54, 55] and 1.2 in 3D [56]. These size ratios are chosen to maintain structural disorder in the bed. In our analysis, we use the average diameter to evaluate dimensionless quantities such as  $\text{Re}_*$ . Our domain has periodic boundaries in the stream-wise direction, as well as in the cross-stream direction in 3D. We use no upper confining boundary and a rigid lower boundary with infinite friction so that the horizontal velocities of all grains touching it are fixed to zero. We integrate

Newton's equations of motion for each grain, including rotational and translation degrees of freedom, using a sixth-order Gear predictor-corrector integration scheme for the case of Cundall-Strack friction [57] for disks in 2D and a modified velocity Verlet integration scheme for all other systems. The total force on each grain is given by the vector sum of contact forces from other grains, a gravitational force, and a drag force from a fluid that moves horizontally, so that

$$m_i \frac{d\vec{v}_i}{dt} = \sum_j \vec{F}_{ij}^c - m_i g' \hat{y} + \vec{F}_f. \quad (5)$$

The total torque on each grain is only due to tangential contact forces, so that

$$I_i \frac{d\vec{\omega}_i}{dt} = \sum_j \vec{s}_{ij} \times \vec{F}_{ij}^c. \quad (6)$$

Here, the sum over  $j$  only includes grains contacting grain  $i$ ,  $\vec{s}_{ij}$  is the vector connecting the center of grain  $i$  to the point of contact between grains  $i$  and  $j$ ,  $m_i \propto D_i^2$  is the mass of the grain,  $I_i$  is the moment of inertia of the grain,  $D_i$  is the diameter of the grain,  $\vec{v}_i$  is the velocity of the grain,  $m_i g'$  is the buoyancy-corrected grain weight, and  $\vec{F}_f$  is the drag force from a model fluid flow, which we discuss below. For the frictionless, elastic case [47],  $\vec{F}_{ij}^c = \vec{F}_{ij}^r$ , where  $\vec{F}_{ij}^r = K \left(1 - \frac{r_{ij}}{D_{ij}}\right) \theta \left(1 - \frac{r_{ij}}{D_{ij}}\right) \hat{r}_{ij}$  is the pairwise (linear repulsive spring) force on grain  $i$  from grain  $j$ , where  $K$  is the grain stiffness,  $r_{ij}$  is the separation between the centers of the grains,  $D_{ij} = (D_i + D_j)/2$ ,  $\hat{r}_{ij}$  is the unit vector connecting their centers, and  $\theta$  is the Heaviside step function. We set the nondimensional stiffness  $\frac{K}{mg'} > 3 \times 10^3$  to be sufficiently large that our results become independent of  $K$ . In this study, we modify the contact force  $\vec{F}_{ij}^c$  to include dissipative grain-grain interactions and tangential forces. The dissipative force is given by  $\vec{F}_{ij}^d = \gamma_v \frac{m_i m_j}{m_i + m_j} (\vec{v}_i - \vec{v}_j) \cdot \hat{r}_{ij}$ , where the dissipation rate  $\gamma_v = \frac{-2 \log e_n}{\tau_c}$ ,  $\tau_c = \frac{\pi \sqrt{m}}{2K}$  is the grain-grain collision time,  $m$  is the mean grain mass, and  $e_n$  is the coefficient of normal restitution [58]. This form for the normal dissipation is often used to model energy losses that arise from contact mechanics, such as viscoelasticity, internal heating, or internal vibrational modes of grains. Here, it is likely that the fluid in the intergrain gap dominates the energy loss during a collision, and the effective  $e_n$  depends on the relative impact velocity of the grains and the viscosity of the fluid [59–61]. We hold  $e_n$  fixed for each individual simulation, independent of the relative grain velocity at contact or local fluid behavior. We will include velocity and viscosity dependence of the coefficient of restitution in future studies.

Tangential forces in granular beds arise via two mechanisms: nonspherical grain shape and microscopic friction. We approximate these two mechanisms using a grain-asperity model [62, 63] and the Cundall-Strack model for friction [57], respectively. In the grain-asperity model, shown in Fig. 4(a)-(b) and Fig. 5(b), we use clusters of  $n$  disks of a fixed size  $d$ . The centers of the disks lie on a circle of radius  $a$ , spaced at angular intervals of  $2\pi/n$ . The non-overlapping area  $A_i$  of each cluster is calculated and the effective diameter for use in setting the fluid drag force is  $D_i = \sqrt{4A_i/\pi}$ . We assume that small disks on each grain cluster interact via purely repulsive linear spring forces. These forces do not generally act through the center of mass of the cluster, and therefore generate torques. (This means that the sum over  $j$  in Eq. (6) now includes multiple contacts between clusters  $i$  and  $j$ .) In this way, macroscopic geometrical friction is introduced via the asperities, as is the case in natural systems, where grains of sand or gravel are almost never spherical.

In the second approach, shown in Figs. 4(c) and 5(c), grains are represented by disks that interact via Cundall-Strack friction [57], which approximates microscopic friction through the use of linear tangential springs at intergrain contacts with tangential force  $F_{ij}^t = -K_t u_{ij}^t$ , where  $K_t = K/3$  and  $u_{ij}^t$  is the relative displacement of the point of contact between grains  $i$  and  $j$ . At each contact, we enforce the Coulomb sliding condition,  $F_{ij}^t \leq \mu F_{ij}^r$ , where  $\mu$  is the static friction coefficient. When  $F_{ij}^t$  exceeds  $\mu F_{ij}^r$ , we set  $u_{ij}^t = \mu F_{ij}^r / K_t$ , and the grains slide relative to each other.

For the case of the grain-asperity model, the value of  $F_{ij}^t / F_{ij}^r$  is determined by local geometry at the points of contact, with  $F_{ij}^t / F_{ij}^r \leq \mu_{\text{eff}}$ , where  $\mu_{\text{eff}}$  corresponds to the case of an asperity from one cluster contacting two asperities from a different cluster. For the Cundall-Strack model, the value of  $F_{ij}^t / F_{ij}^r$  depends on the history of the contact, i.e., the accumulated tangential displacement  $u_{ij}^t$ . Figure 4 shows a comparison of packings generated with  $\mu = \mu_{\text{eff}} = 0.6$ . The distributions of  $F_{ij}^t / F_{ij}^r$  are similar for the two models; both have a maximum near 0.6 and a broad distribution below the maximum. (Note that  $\mu_{\text{eff}}$  for contacts between two clusters of the same size is 0.6, whereas  $\mu_{\text{eff}}$  can be larger for an asperity from a small grain that is in contact with a asperities on a large grain.)

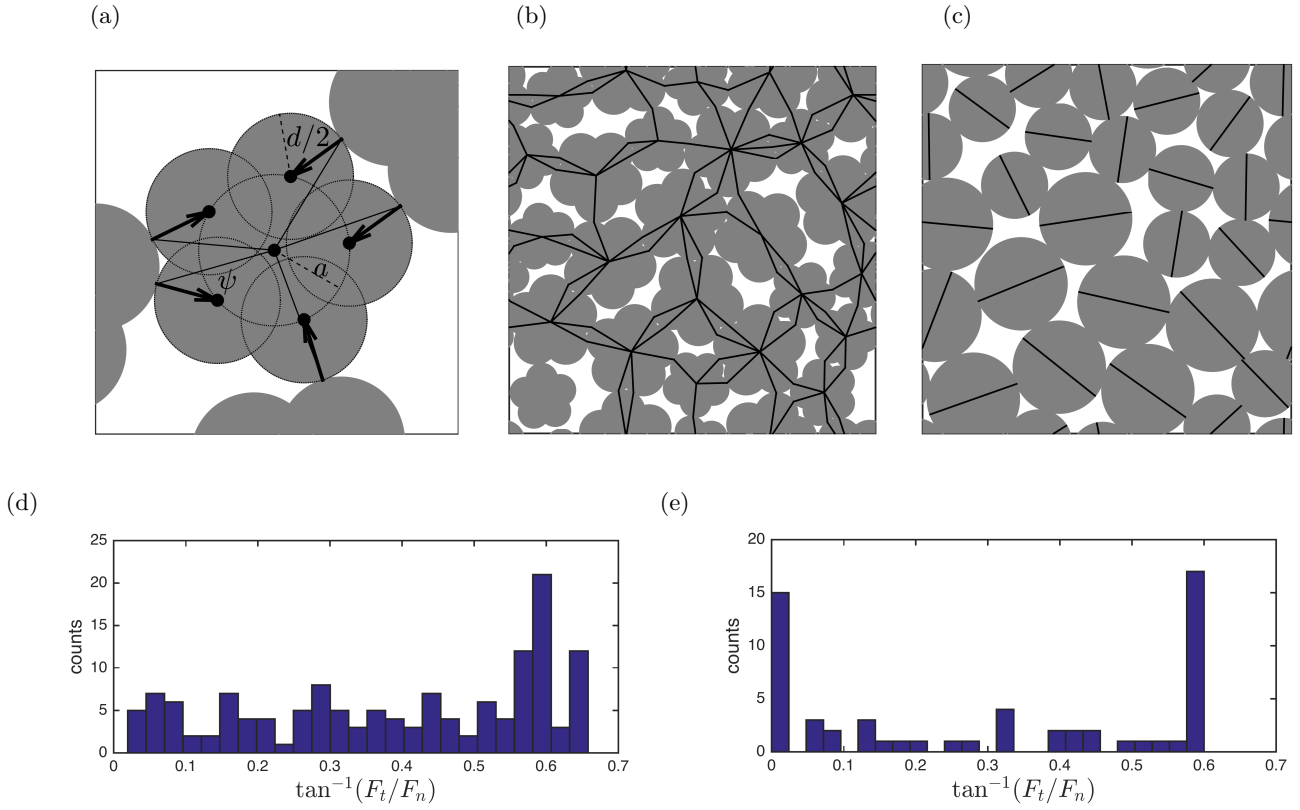


FIG. 4. (a) A depiction of the grain-asperity model [62, 63]. Grain clusters are composed of  $n$  frictionless disk-shaped asperities, each with diameter  $d$ , with their centers regularly spaced on a circle of radius  $a$ . Arrows show the direction of contact forces, and solid lines connect the contact point to the center of the cluster. The angle  $\psi$  between the arrows and solid lines sets the ratio of tangential  $F_t$  and normal  $F_n$  components of the contact forces, and thus the maximum ratio  $\max(F_{ij}^t/F_{ij}^r) = \mu_{\text{eff}}$  is set purely by geometry. (b,c) Packings constructed from (b) grain clusters and (c) disk-shaped grains with Cundall-Strack friction [57], both containing 25 grains, using an athermal packing generation protocol [64]. Grain clusters shown here have  $n = 5$  and  $a/d = 0.6$ , which gives  $\mu_{\text{eff}} = 0.6$  for two grains of the same size. The center grain in panel (a) is contacting the grain to its left with  $F_{ij}^t/F_{ij}^r = \mu_{\text{eff}}$ . The disk-shaped grains with Cundall-Strack friction have  $\mu = 0.6$  to match the grain clusters. Panels (d) and (e) show histograms of the ratio  $F_{ij}^t/F_{ij}^n$  for all contact forces in (b) and (c), respectively.

TABLE I. A list of the characteristics for different simulations of the grain-asperity model, where  $n$  is the number of disk-shaped asperities per grain,  $a/d$  is the distance from the center of each disk-shaped asperity to the center of the grain, and  $\mu_{\text{eff}}$  is the maximum ratio of  $F_{ij}^t/F_{ij}^n$ .

$n$	$a/d$	$\mu_{\text{eff}}$
2	0.1	0.2
2	0.2	0.42
2	0.4	1.06
3	0.2	0.33
3	0.4	0.7
3	0.5	0.93
3	0.75	2
4	0.5	0.65
4	0.75	1.1
4	1	2
5	0.1	0.11
5	0.4	0.4
5	0.6	0.6



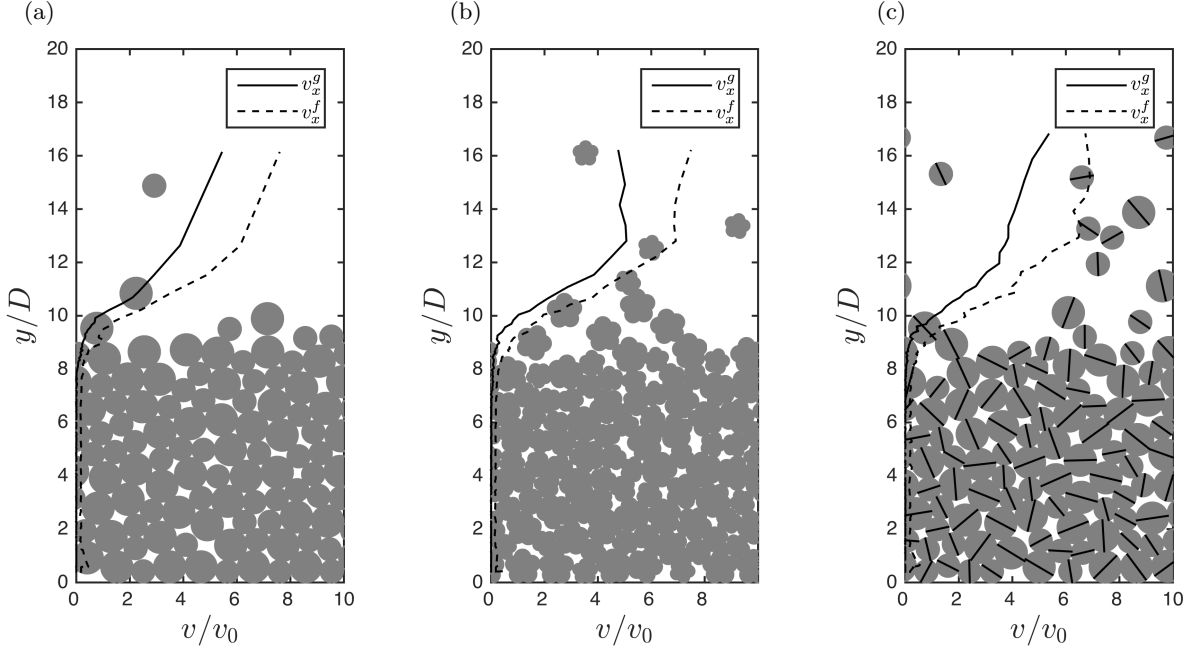


FIG. 5. Panels (a-c) show snapshots of simulations using (a) frictionless disks; (b) grain clusters from Fig. 4 with  $\mu_{\text{eff}} = 0.6$ ; and (c) disks with Cundall-Strack friction [57], with  $\mu = 0.6$ . All three simulations shown here are at  $\Theta = 0.25$  and  $\text{Re}_p \approx 1.6$ , with  $e_n = 0.8$ . The vertical axis gives the height  $y/D$  above the lower boundary, where  $D$  is the grain diameter, and the horizontal axis gives the horizontal velocity  $v_x/v_0$  of grains and the fluid, where  $v_0$  is the characteristic fluid velocity at the bed surface. Solid and dashed lines show the time-averaged horizontal component of grain velocity  $v_x^g$  and fluid velocity  $v_x^f$ , respectively, during a short simulation.

### B. Details of the fluid drag

To simulate fluid shear, we choose a model fluid velocity profile that acts primarily on the surface grains of a static bed and that increases somewhat for mobilized grains that move above the surface. We set a characteristic fluid velocity  $v_0$  at the surface of a static bed, and we multiply this velocity by a fluid profile  $f(\vec{r})$  according to the local packing fraction of grains  $\phi_i$ , which yields  $v_0 f(\vec{r})$  as the fluid velocity at  $\vec{r}$ . In 2D,  $f(\phi_i) = e^{-b(\phi_i - \phi_t)}$ , where  $b$  controls the ratio of the magnitude of the fluid flow above and inside the bed and  $\phi_t = 0.5$  is the typical packing fraction of a grain at the top of a static 2D bed.  $\phi_i$  is calculated in a small circular region with diameter  $D_i + 2D_l$  around the center of each grain, where  $D_l$  is the diameter of the larger grains. Since  $f = 1$  for  $\phi_i = \phi_t$ ,  $v_0$  is roughly equal to the fluid velocity at the free granular surface. In 3D, we use a modified form,  $f(\phi_i) = [\exp(-b\phi) - \exp(-b\phi_m)] / [\exp(-b\phi_t) - \exp(-b\phi_m)]$ , as shown in Fig. 6.  $\phi_m = 0.7$  approximates the maximum packing fraction in the bulk of the bed, and  $\phi_t = 0.42$  is the typical packing fraction of a grain at the top of the bed. This modified form is used to sufficiently reduce the fluid velocity inside a 3D bed, where typical packing fractions are much smaller ( $\approx 0.55 - 0.64$ ) than in 2D ( $\approx 0.75 - 0.84$ ). For all simulations, we set  $b = 5$ . We find that our results are insensitive to the choice of  $f$ , provided its magnitude is very small in the bed.

We then set the fluid force  $\vec{F}_f$  from Eq. (5) equal to the form from Eq. (2):

$$\vec{F}_f = B_1(v_0 f(\vec{r}) \hat{x} - \vec{v}_i) + B_2|v_0 f(\vec{r}) \hat{x} - \vec{v}_i|(v_0 f(\vec{r}) \hat{x} - \vec{v}_i). \quad (7)$$

In addition to  $\frac{K}{mg'}$ ,  $\mu$ , and  $e_n$ , which determine grain-grain interactions, Eqs. (5)-(7) include three additional nondimensional numbers:

$$\Theta = \frac{2}{3} \left( \frac{B_1}{mg'} v_0 + \frac{B_2}{mg'} v_0^2 \right) \quad (8)$$

$$\Gamma = \frac{B_1/m}{\sqrt{g'/D}} \quad (9)$$

$$\text{Re}_p^0 = \frac{60 B_2 v_0}{B_1}. \quad (10)$$

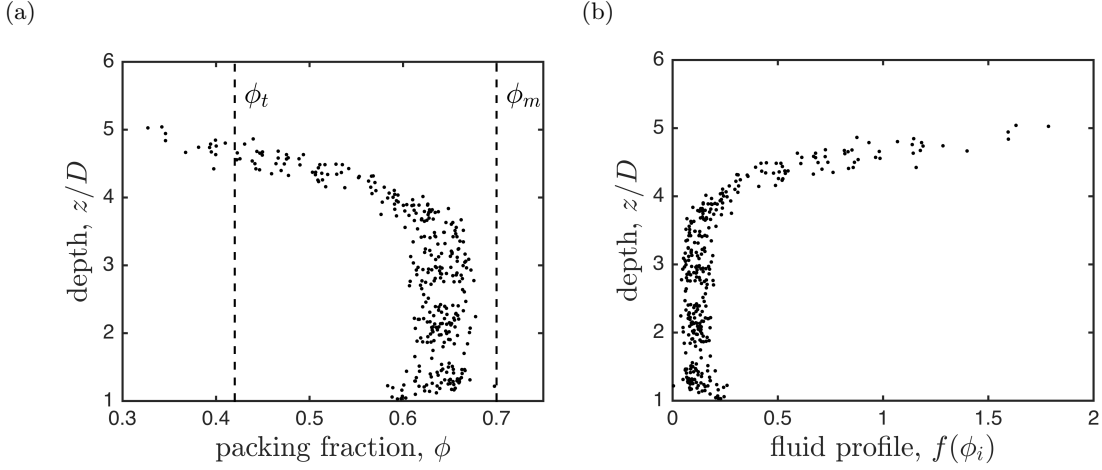


FIG. 6. (a) A scatter plot of the height  $z/D$  of each grain above the lower boundary versus the packing fraction  $\phi$  of a typical configuration of 400 grains in a static, 3D bed.  $\phi_t = 0.42$  and  $\phi_m = 0.7$  are marked with dashed lines. (b) A plot of the same data points in (a), but evaluated in the fluid profile function used for 3D simulations,  $f(\phi_i) = [\exp(-b\phi) - \exp(-b\phi_m)] / [\exp(-b\phi_t) - \exp(-b\phi_m)]$ , with  $b = 5$ .

$B_1$  and  $B_2$  are proportional to  $D_i$  and  $D_i^2$ , respectively, but we use the mean value of  $D$  in our dimensional analysis.  $\Theta$  gives the dimensionless shear stress at the top of a static bed. The factor  $2/3$  represents a conversion [29] from a force ratio, which we assign in simulations, to the stress ratio  $\Theta = \frac{\tau}{\rho g' D}$ . The fluid stress  $\tau$  acts approximately over the cross-sectional area of a sphere,  $A = \frac{\pi}{4} D^2$ , and  $\tau A$  is the horizontal fluid force. The gravitational stress  $\rho g' D$  acts over an effective area  $\frac{V}{D} = \frac{\pi}{6} D^2$ , and  $\rho g' D \frac{V}{D}$  is the grain weight. Thus, the explicit force ratio, which we assign in simulations, is converted to a stress by multiplying by  $\frac{V}{AD} = \frac{2}{3}$ .  $\Gamma$  is the ratio of the gravitational time scale  $\tau_g = \sqrt{D/g'}$  to the characteristic viscous time  $m/B_1$  for grains to equilibrate to the local fluid velocity. Thus,  $\text{Re}_* \propto \sqrt{\Theta}/\Gamma = \tau_\nu/\tau_\Theta$ .  $\text{Re}_p^0$  is the particle Reynolds number of a grain at the surface of the bed, which determines the relative contributions of the viscous and inertial drag terms. (The numerical value of 60 in the numerator of  $\text{Re}_p^0$  follows from taking the ratio of the linear and quadratic drag terms in Eq. (2).) For simulations with linear drag, we set  $\text{Re}_p = B_2 = 0$  and vary only  $\Gamma$  and  $\Theta$ . However, we also show results with a viscous-plus-inertial drag law, where we vary  $\text{Re}_p^0$  and  $\Theta$ . In this case,  $\Gamma$  is not set independently, but it is constrained by the ratio  $\rho_g/\rho_f = \frac{3m}{10B_2 D}$ , which we set to 3. Thus, in simulations,  $\text{Re}_* = \sqrt{3\Theta}/\Gamma$ , according to equation (4). We emphasize that, when comparing results for linear and quadratic drag laws, we first assign  $\Theta$  and then specify  $v_0$ . Simulations for linear and quadratic drag laws at the same  $\Theta$  will require different values of  $v_0$ . This is distinct from the case where the fluid velocity is specified, in which case we would severely underestimate the stresses at high  $\text{Re}_*$ .

To characterize the onset and cessation of bed motion in our system, we employ two protocols. To study the mobile-to-static transition defined by  $\Theta_c$ , we distribute all grains randomly on a cubic lattice throughout the domain and set a constant value of  $\Theta$  for a total time of roughly  $10^6$  grain-grain collision times (our results are insensitive to the details of this initial condition, as long as we consider large ensembles of initial conditions where a significant fraction of grains are suspended when the model fluid flow is applied). We then observe if and when our system stops, which we define as when the maximum acceleration  $a_{\max} < a_{\text{thresh}}$  and maximum velocity  $v_{\max} < v_{\text{thresh}}$ , where  $a_{\text{thresh}}$  is roughly one order of magnitude smaller than  $g'$  and roughly three orders of magnitude smaller than typical values for a moving bed and  $v_{\text{thresh}}$  is roughly three orders of magnitude smaller than the fluid velocity at the surface. (Our results are independent of the values of these thresholds, provided they are sufficiently small.) To understand the dynamics of the static-to-mobile transition, we begin with a static bed and slowly increase  $v_0$  in small increments, corresponding to increases in stress  $\Delta\Theta \leq 0.05\Theta$  until we observe  $a_{\max} > a_{\text{thresh}}$  or  $v_{\max} > v_{\text{thresh}}$ . We then keep  $v_0$  constant until  $a_{\max} < a_{\text{thresh}}$  and  $v_{\max} < v_{\text{thresh}}$  or until the end of our simulation. We perform simulations spanning  $10^{-2} < \text{Re}_* < 10^4$  for linear and quadratic drag laws with varying grain-grain interactions.

#### IV. RESULTS

The main result from our work is shown in Figure 7. The small, black dots represent experimental and field data from Dey [4]. The black curve with square markers is the boundary  $\Theta_c(\text{Re}_*)$  between systems with and without

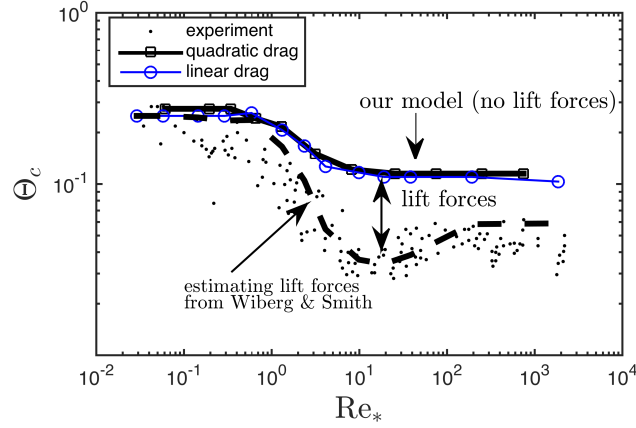


FIG. 7. A collection of experimental and field data (filled dots) from Dey [4] showing the variation of the minimum Shields number for grain motion  $\Theta_c$  with  $Re_*$ . The solid curves show the boundaries between states with and without sustained grain motion from our model, which excludes lift forces. The black curve with square markers shows results for quadratic drag, and the blue curve with open circles shows results for linear drag in the limit of small restitution coefficient. The dashed curve is constructed by multiplying our results by the curve  $T(Re_*)$  shown in Fig. 2, from Wiberg and Smith [29], to estimate lift forces.

sustained grain motion from our model using quadratic drag. We find a nearly identical boundary using a linear drag law when  $e_n$  is small, as shown by the solid blue curve with open circles, where  $e_n = 0.2$ . As discussed in our results below, small  $e_n$  suppresses the effect of grain impact with the bed for linear drag; for quadratic drag, the inertial equilibration time scale limits the kinetic energy of mobilized grains. In both the cases of linear drag with small  $e_n$  and quadratic drag, the key physics near  $\Theta_c$  is the dynamics of mobilized grains between successive interactions with the bed.

Since we use a model fluid flow that does not depend on  $Re_*$ ,  $Re_*$ -dependent grain dynamics are solely responsible for the variation seen in Fig. 7. Figure 8 shows data from simulations of mobilized beds using quadratic drag at  $\Theta \approx \Theta_c(Re_*)$  for  $10^{-2} \leq Re_* \leq 10^3$ . Figure 8(a) shows height  $z/D$  versus packing fraction  $\phi$ , and the inset shows the maximum height  $z_{\max}$  that mobile grains achieve as a function of  $Re_*$ . Figure 8(b) shows height  $z/D$  versus grain velocity  $v_g/v_0$  (solid lines) and fluid velocity  $v_f/v_0$  (dashed lines). The inset shows the ratio of average grain velocity  $\bar{v}_g$  in the top layer and above (i.e.,  $z/D > 5.25$ ) to the average fluid velocity  $\bar{v}_f$  in the same region. As  $Re_*$  increases,  $\bar{v}_g/\bar{v}_f$  decreases, meaning that mobile grains do not equilibrate to the fluid flow. Figure 8(c) shows the height  $z/D$  versus the normalized horizontal grain acceleration  $a_g(\Theta g')^{-1}$ . At small  $Re_*$ , grain acceleration is negligible, and mobile grains always move with the local fluid flow. At high  $Re_*$  grains are significantly accelerated, and their momentum is lost through collisions with the bed, which is indicated by the negative acceleration peak at the bed surface for  $Re_* \approx 250$  (green stars). The inset shows the average normalized horizontal grain acceleration  $\bar{a}_g(\Theta g')^{-1}$  in the top layer and above ( $z/D > 5.25$ ) as a function of  $Re_*$ . As  $Re_*$  increases, average normalized horizontal grain acceleration for mobilized grains increases until it plateaus for  $Re_* > 10$ . Together these data show how grain dynamics vary with  $Re_*$  from viscous-dominated at low  $Re_*$  to acceleration-dominated at high  $Re_*$ , as discussed in Sec. II.

Our results for  $\Theta_c(Re_*)$  in Fig. 7 display plateaus at low and high  $Re_*$ , denoted  $\Theta_c^l$  and  $\Theta_c^h$ , respectively. The behavior of the Shields curve at  $Re_* < 1$  is currently an open question. Most hydraulic models [22, 23, 27] assume a decreasing trend of  $\Theta_c(Re_*)$  for  $Re_* < 10$ . In simulations, we observe a plateau with  $\Theta_c^l \approx 0.28$  [48]. We interpret this plateau as the shear force corresponding to the most geometrically stable arrangement of the bed, suggesting that configurations that can resist  $\Theta > \Theta_c^l$  do not exist. For  $Re_* \gg 1$ ,  $\Theta_c$  also displays a plateau  $\Theta_c^h$  that has the same value for linear and quadratic drag laws, meaning that the minimum stress required to maintain grain motion in these simulations is the same for these two cases, and is not controlled by the form of the drag law. The agreement of the plateau values for the linear and quadratic drag laws suggests that, in our model near  $\Theta_c$  at  $Re_* \gg 1$ , the dynamics are determined by mobile grains hopping along the bed, with roughly constant acceleration  $a \sim \Theta g'$  between collisions with the bed.

With this simple model, our results do not quantitatively capture the global minimum in the Shields curve at  $Re_* \approx 10$ , and we overestimate  $\Theta_c$  by roughly a factor two at high  $Re_*$ . However, in this model we neglected lift forces and turbulence, and thus we expect to overpredict  $\Theta_c$  in this regime. For instance, as we discussed in the introductory section, using the results from Wiberg and Smith [29] to approximate lift forces gives good quantitative

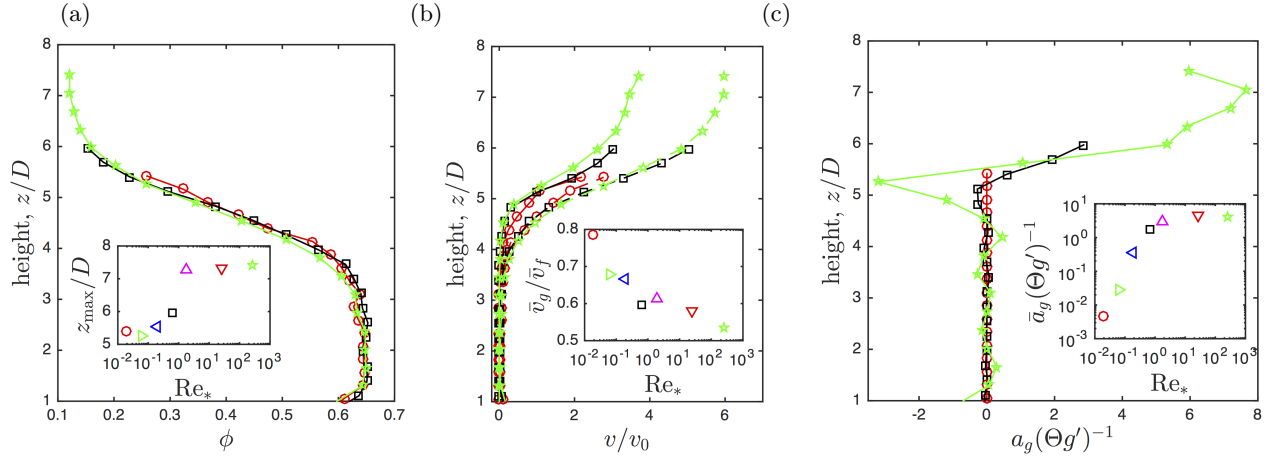


FIG. 8. Packing fraction, grain and fluid velocity, and grain acceleration profiles from simulations of mobilized beds using a quadratic drag law at  $\Theta \approx \Theta_c(\text{Re}_*)$  and  $10^{-2} \leq \text{Re}_* \leq 10^3$ . The profiles are obtained by time-averaging and binning by grain height  $z/D$  (vertical axes) for  $\text{Re}_* \approx 0.02$  (circles), 0.7 (squares), and 250 (stars), with more values included in the insets. (a) Packing fraction  $\phi$  profile for several  $\text{Re}_*$ . The inset shows the maximum grain height  $z_{\text{max}}$  versus  $\text{Re}_*$ . (b) Grain  $v_g/v_0$  (solid lines) and fluid  $v_f/v_0$  (dashed lines) velocity profiles. The inset shows the ratio of the average grain velocity  $\bar{v}_g$  in the mobilized region and above to the average fluid velocity  $\bar{v}_f$  in the same region. The mobilized region is defined as  $z/D > 5.25$  and the results are qualitatively insensitive to the choice of the threshold. (c) Normalized horizontal grain acceleration  $a_g(\Theta g')^{-1}$  profile. The inset shows the average normalized horizontal grain acceleration in the mobilized region versus  $\text{Re}_*$ .

agreement between our results and the experimental data. To approximate lift forces, we multiply the values of  $\Theta_c$  at each  $\text{Re}_*$  in our simulations with the value at the same  $\text{Re}_*$  of the scaling function  $T(\text{Re}_*)$ , defined in Eq. (1) and depicted in Fig. 2(b), for monodisperse sediment. This gives the dashed line in Fig. 7 that agrees well with the Shields curve.

Below, we show that we find qualitatively similar behavior in 2D, although the numerical values for  $\Theta_c$  increase by roughly a factor 2. Thus, with regard to grain dynamics, 2D and 3D show slight quantitative difference, but are qualitatively the same. We interpret the increase in  $\Theta_c$  from 3D to 2D to follow from the fact that the energy landscape of a 2D bed is more difficult for grains to navigate, as grains must roll over obstacles instead of traversing the low points between impeding grains. This raises important questions about whether and how quasi-2D calculations of pocket angles relate to 3D systems. Using 2D simulations, we show that the boundary  $\Theta_c$  is insensitive to friction, irregular grain shape, and the details of the fluid flow (provided it is very small deep in the bed). Additionally, concerning the initiation of grain motion in a static bed, we show that the onset of grain motion always occurs at  $\Theta = \Theta_c$  in the limit of large systems (see Sec. IV C).

### A. Comparing linear and quadratic drag laws

In this section, we show results from 3D simulations with linear and quadratic drag laws. We show that the boundary between mobile and static states is the same for linear and quadratic drag laws, provided  $e_n$  is small when a linear drag law is used. Also, the sediment transport rate shows the same dependence on  $\Theta$  for linear and quadratic drag laws. At  $\text{Re}_* \gg 1$ , this is only possible if grain motion near  $\Theta_c$  is dominated by nearly constant acceleration dynamics between interactions with the bed and not the form of the drag law.

Figure 9 shows the boundaries between systems with and without sustained grain motion for quadratic and linear drag laws. The thick black line with square markers shows the boundary between systems with and without sustained grain motion using a quadratic drag law, representing both the transitions from a mobile to a static bed as well as from a static to a mobile bed (i.e., we observe no hysteresis for a quadratic drag law). This boundary is independent of  $e_n$ . The thin, colored lines with circle markers show the minimum  $\Theta$  required to sustain grain motion indefinitely, using a linear drag law. The different colors (red, green, black, blue, magenta) represent different restitution coefficients ( $e_n = 0.9, 0.8, 0.5, 0.2$ , and  $0.1$ ). As  $e_n \rightarrow 0$ , these boundaries form a single curve, with plateaus  $\Theta = \Theta_c^l \approx 0.28$  and  $\Theta = \Theta_c^h \approx 0.11$  at low and high  $\text{Re}_*$ , respectively. The dashed, black line represents  $\Theta_0^h$ , which is the minimum  $\Theta$  required to *initiate* sustained grain motion from a static bed at  $\text{Re}_* \gg 1$ . As we show in Section IV C, sustained grain motion is always initiated at this value in the large-system limit. We find that  $\Theta_0^h$  is insensitive to the drag law and restitution coefficient.

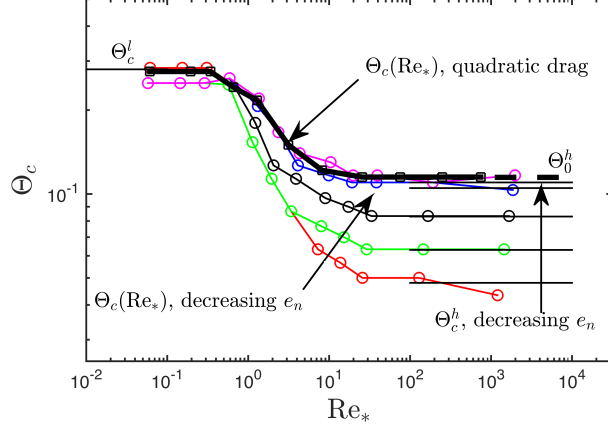


FIG. 9. The solid black curve with square markers is  $\Theta_c(\text{Re}_*)$  with the quadratic drag law. The thin curves with open circles represent  $\Theta_c(\text{Re}_*)$  for linear drag with  $e_n = 0.9$  (red), 0.8 (green), 0.5 (black), 0.2 (blue), and 0.1 (magenta). Plateau values  $\Theta_c^l$  and  $\Theta_c^h$  for the curves from a linear drag law are marked with thin black lines. The thicker, dashed line shows  $\Theta_0^h$ , which is the minimum  $\Theta$  at  $\text{Re}_* \gg 1$  required to initiate sustained grain motion for linear and quadratic drag for all values of  $e_n$ . As we discuss in Section IV C, grain motion at  $\text{Re}_* \gg 1$  is always initiated at this boundary for large systems. As  $e_n \rightarrow 0$ ,  $\Theta_c^h \rightarrow \Theta_0^h$  for a linear drag law.

Figure 10 shows representative data for  $\text{Re}_* \ll 1$ , where agreement is expected between the linear and quadratic drag laws. As discussed in Section III B, we begin with a mobilized system, where grains are suspended, and apply the model fluid flow.  $\Theta_c$  is characterized by a grain discharge per unit width that tends to zero and diverging stopping times for  $\Theta$  just below  $\Theta_c$ . We characterize the grain motion by plotting  $q/\sqrt{g'D^3}$ , where  $q$  is the discharge per unit width. The dashed curves in Fig. 10(a) show  $q/\sqrt{g'D^3}$  at different times (blue to red represents increasing time), where each data point is obtained from an ensemble of ten simulations. Each data point with a nonzero  $q$  means that in at least half of the simulations the grains did not stop, and the value of  $q$  represents the average of all simulations where grains were still in motion. The solid black curve is the steady-state discharge per unit width at the end of the simulation. If in at least half of the simulations, the grains stopped, we measure the average time  $t_s$  that it took the grains to stop moving. Figure 10(b) shows  $(t_s - t_{s,0})\sqrt{g'/D}$  plotted versus  $\Theta$ , where  $t_{s,0}$  is the stopping time for  $\Theta \rightarrow 0$ . The black curve with filled square markers represents the data for the quadratic drag law, and the red curve with open circle markers represents the data for the linear drag law with  $e_n = 0.9$ . The stopping time diverges and  $q$  tends to zero at roughly the same value of  $\Theta = \Theta_c^l \approx 0.28$ . All data shown in Fig. 10 are insensitive to  $e_n$  and to the form of the drag law. At  $\text{Re}_* \ll 1$ , the dynamics for linear and quadratic drag laws are the same, and thus good agreement for  $\Theta_c$  is expected in this regime. Additionally, we find that all data shown in Fig. 10 are insensitive to  $\text{Re}_*$  for  $\text{Re}_* \ll 1$ , provided that time scales are normalized by the viscous time  $\tau_\nu$ . This means that  $q$  scales with  $v_0$  in this regime, since mobile grains quickly equilibrate to the local fluid speed.

Figure 11 shows similar data for  $\text{Re}_* \gg 1$ , where the agreement between the linear and quadratic drag laws is much more surprising. As before,  $\Theta_c$  is obtained by finding the stress at which the grain flux tends to zero and the stopping time diverges. Figure 11(a) again shows  $q$  for increasing times, where data points are calculated in the same way as for  $\text{Re}_* \ll 1$ . Dashed curves represent increasing times (blue to red), and the solid black curve represents the steady state grain flux (measured at the end of the simulation). Figure 11(b) shows  $(t_s - t_{s,0})\sqrt{g'/D}$  plotted versus  $\Theta$  for quadratic (thick black line with filled squares) and linear (thin lines with open circles) drag laws. Figure 11(c) shows  $q$  versus  $\Theta$  for quadratic and linear drag laws. As before,  $q$  tends to zero and  $t_s$  diverges at roughly the same value of  $\Theta$ . As  $e_n \rightarrow 0$  for linear drag, the critical  $\Theta$  approaches the value for the quadratic drag law,  $\Theta = \Theta_c^h \approx 0.11$ .

Thus, at  $\text{Re}_* \gg 1$ , we find that using linear (with small  $e_n$ ) and quadratic drag laws give the same value of  $\Theta_c$  as well as the same dependence of  $q$  versus  $\Theta$ . This insensitivity to the drag law is only possible if mobilized grains remain very close to the bed (i.e., bed load transport). Under a linear (viscous only) drag law, grains can be accelerated to much larger speeds, since  $\tau_\nu \propto \text{Re}_*$  for all  $\text{Re}_*$ . Thus, for  $\text{Re}_* \gg 1$  if mobilized grains rebound high above the bed, they will be accelerated over their full trajectory. As shown in Fig. 11(c), for linear drag with  $\Theta$  near  $\Theta_c$  and small  $e_n$ , we observe agreement with the case of quadratic drag. As  $\Theta$  becomes larger, grains rebound higher into the fluid flow. These grains will deliver significant energy when they impact the bed and, more importantly, they will rebound to large heights above the bed. These effects are suppressed when  $e_n$  is small and  $\Theta$  is near  $\Theta_c$ , and the behavior of  $q(\Theta)$  for linear drag approaches the  $q(\Theta)$  curve for quadratic drag as  $e_n \rightarrow 0$ . In this case, the trajectory of mobilized

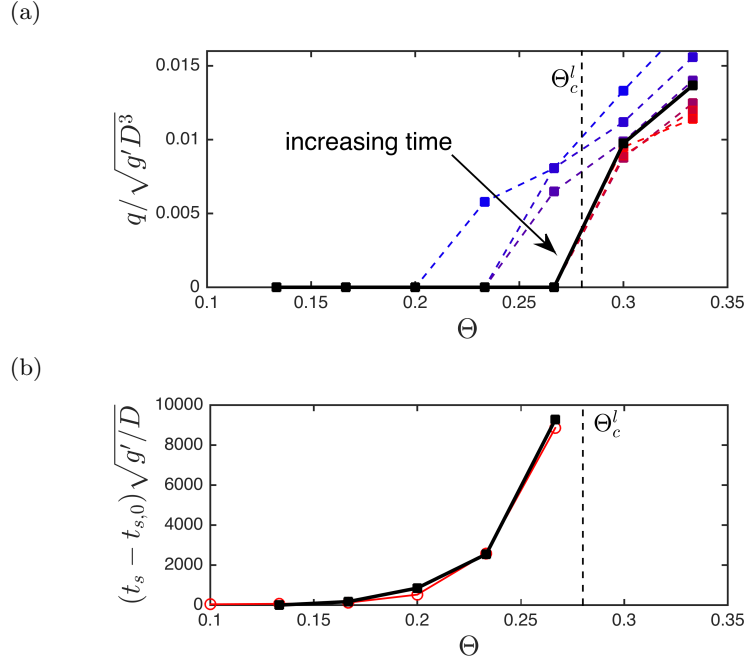


FIG. 10. For simulations with  $\text{Re}_* \ll 1$ , the dimensionless volumetric grain flux per cross stream width  $q / \sqrt{g'D^3}$  (a) and the dimensionless stopping time  $(t_s - t_0) \sqrt{g'/D}$  (b) are plotted versus  $\Theta$ . Data in (a) represents the ensemble average over 10 systems with quadratic drag, where the data are averaged over all systems that were still in motion at increasing time during the simulation. Intermediate times are given by blue to red dashed lines with square markers, and the black line represents the end of the simulation. If more than half of the simulations had stopped, then  $q = 0$ . Data in (b) represent the mean stopping time for ensembles where grain motion ceased in at least half of the simulations. Curves show quadratic (black line with square markers) and linear (red line with open circle markers) drag laws, both with  $e_n = 0.9$ .

grains is confined to positions near the bed, and viscous and inertial drag laws yield the same behavior very close to  $\Theta_c$ , as grain motion is dominated by nearly constant acceleration between collisions with the bed.

## B. Comparison of 2D and 3D systems

In this section, we present results for 2D systems. In 2D, we find a boundary  $\Theta_c(\text{Re}_*)$  similar to that shown in Fig. 7, but the numerical values of  $\Theta_c$  are roughly a factor two larger in 2D compared to 3D. We attribute this difference to the different potential energy landscape at the surface of a rough bed, where mobile grains in 2D must roll over neighboring grains, unlike in 3D where they can pass between neighboring grains. We use 2D simulations to show that  $\Theta_c(\text{Re}_*)$  is only weakly dependent on friction, irregular grain shape, and the details of the applied fluid flow.

In previous studies [47] of frictionless, elastic disks, we found the behavior near  $\Theta_c$  to be nearly independent of system size. Thus, here we compute dynamics using a linear drag law for a large number (roughly 2000) of relatively small systems (200 grains, with stream-wise length  $20D$  and fill height  $10D$ ) to estimate the plateau values  $\Theta_c^l$  and  $\Theta_c^h$  over a large parameter space defined by the restitution coefficient  $e_n$ , the fluid flow profile (determined by  $b$ ), and static friction coefficient  $\mu$  (microscopic friction) or  $\mu_{\text{eff}}$  (grain-asperity model). We vary  $\Gamma$  between 5 and 0.005, and for each  $\Gamma$  we vary  $\Theta$  near the estimated  $\Theta_c(\text{Re}_*)$  in steps of  $\Delta\Theta$  that are no more than 5% of our final measurement of  $\Theta_c$ . (This gives an estimate of our uncertainty in  $\Theta_c$ .) As above, we find plateaus  $\Theta_c^l$  and  $\Theta_c^h$  that characterize cessation of grain motion at low and high  $\text{Re}_*$ , respectively. As above, we also find that  $\Theta_0^h$ , the minimum value of  $\Theta$  at  $\text{Re}_* \gg 1$  to initiate sustained grain motion, is larger than  $\Theta_c^h$ . We again find that this hysteresis is an artifact of saltating grains obtained using a linear drag law, and  $\Theta_c^h \rightarrow \Theta_0^h$  as  $e_n \rightarrow 0$ .

Figure 12 and Table II give results for frictionless disks, with  $e_n = 1$ , where the fluid flow profile  $f(\phi_i) \propto e^{-b\phi_i}$  is controlled by varying  $b$ . We note that for  $b \geq 5$ , the flow inside the bed is sufficiently small that  $\Theta_c^l$  is independent of  $b$  (that is, stability at low  $\text{Re}_*$  is dominated by the top layer of grains). This regime corresponds to a fluid force in the bulk of the bed that is at least 5 times weaker than at the surface, a condition that is certainly met in experiments and in nature.  $\Theta_0^h$  is nearly independent of  $b$ .  $\Theta_c^h$  depends strongly on  $b$ , since mobilized grains above the bed will obtain

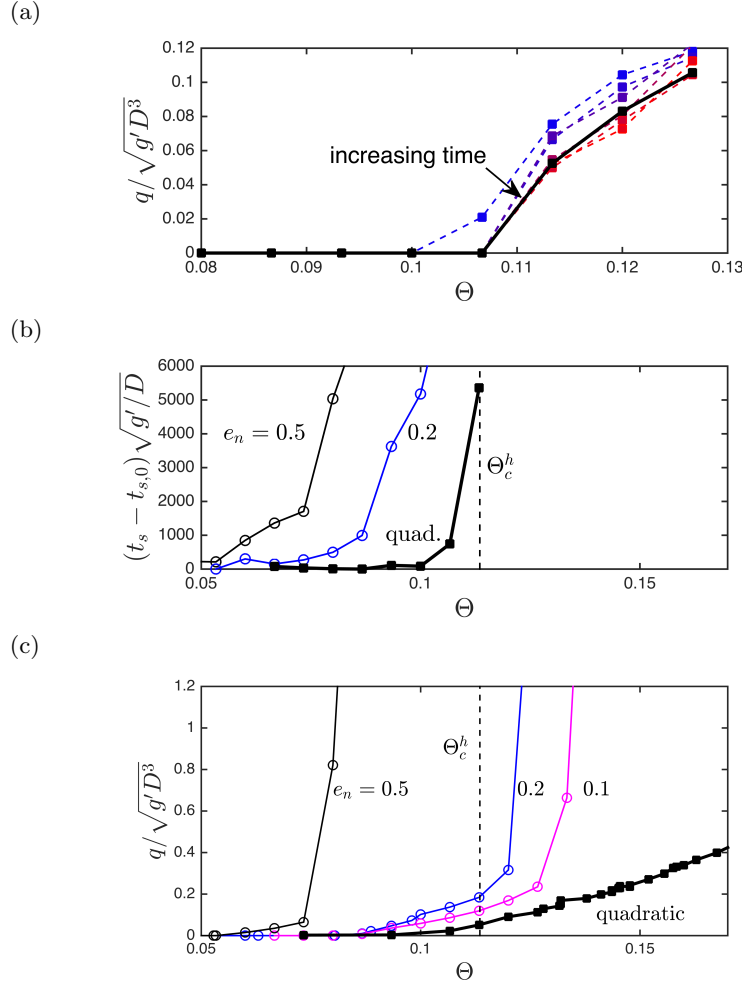


FIG. 11. For simulations with  $\text{Re}_* \gg 1$ , the dimensionless volumetric grain flux per cross stream width  $q/\sqrt{g'D^3}$  (a) and the dimensionless stopping time  $(t_s - t_0)\sqrt{g'/D}$  (b) are plotted versus  $\Theta$ . Data in (a) represents the ensemble average over 10 systems with quadratic drag, computed in the same way as in Fig. 10(a). Blue to red dashed curves represent increasing time, and the solid black curve represents the end of the simulations. Data in (b) is also computed in the same way as in Fig. 10(b), with quadratic (black squares) and linear drag laws with  $e_n = 0.5$  (black open circles) and 0.2 (blue open circles). Additionally, in (c), we compare the grain flux versus  $\Theta$  for the cases of linear and quadratic drag, where we also include the flux for  $e_n = 0.1$  (magenta open circles). Despite the fact that the drag laws have different forms, the curve  $q(\Theta)$  approaches the quadratic case near  $\Theta_c$  as  $e_n \rightarrow 0$ .

more energy for larger fluid flow above the bed. However, as we demonstrated above in the 3D case, this hysteresis is an artifact of linear drag with large restitution coefficient, and  $\Theta_c^h$  increases and the hysteresis disappears when a quadratic drag law is used or when  $e_n \rightarrow 0$  using linear drag.

Figure 13 confirms this for 2D, using results for frictionless disks with  $b = 5$  and varying  $e_n$ . As we decrease  $e_n$ , we observe that  $\Theta_0^h$  and  $\Theta_c^l$  are unchanged, meaning that the values associated with these plateaus do not depend on the elasticity of grain-grain collisions. However, as  $e_n$  decreases,  $\Theta_c^h$  increases and approaches  $\Theta_0^h$ , so that the size of the hysteresis  $\Theta_c^h - \Theta_0^h$  decreases with restitution coefficient  $e_n$ . As  $e_n$  approaches zero, mobilized grains undergo perfectly inelastic collisions with the bed, meaning that, as above in 3D, they do not rebound into the larger fluid flow and they become much less efficient in mobilizing additional grains. Thus, as before,  $\Theta_c^h = \Theta_0^h$  when physically unrealistic effects from the linear drag law are suppressed. We note that small  $e_n$  may actually be more realistic [59–61], since collisions between grains that would yield large  $e_n$  in dry collisions can have very small  $e_n$  when the collisions are mediated by a viscous fluid.

Figure 14 shows the values of the plateaus  $\Theta_c^l$  and  $\Theta_c^h$  with  $b = 5$  and small  $e_n$ .  $\Theta_c^l$  and  $\Theta_c^h$  are plotted as a function of the friction coefficient  $\mu$  for disks with Cundall-Strack friction and the effective friction coefficient  $\mu_{\text{eff}}$  for grain clusters (see Table I). Circles represent disks with Cundall-Strack friction, with a friction coefficient  $\mu$ . Other symbols

TABLE II. The flow velocity ratios and plateau values  $\Theta_c^l$ ,  $\Theta_c^h$ , and  $\Theta_0^h$  (see Fig. 9) for frictionless elastic disks as a function of the fluid decay constant  $b$ .  $v_a$ ,  $v_0$ , and  $v_b$  are the fluid velocities above the bed, at the surface of the bed, and in the interior of the bed, respectively.

$b$	$v_a/v_0$	$v_0/v_b$	$\Theta_c^l$	$\Theta_c^h$	$\Theta_0^h$
2	2.2	2.0	0.5	0.09	0.19
4	5.0	3.9	0.66	0.1	0.23
5	7.4	5.5	0.9	0.06	0.22
6	11.0	7.7	0.9	0.02	0.2

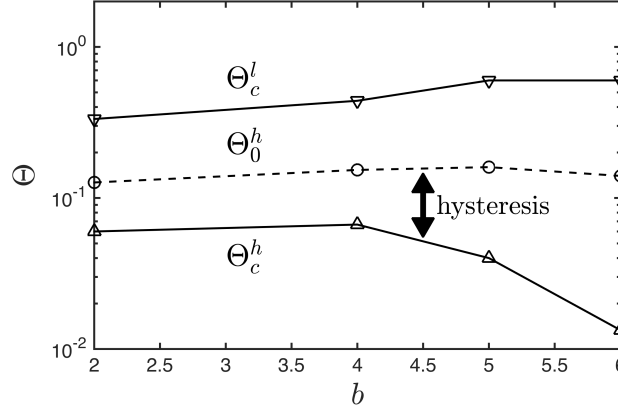


FIG. 12. A plot of the plateau values  $\Theta_c^l$ ,  $\Theta_0^h$ , and  $\Theta_c^h$  (see Fig. 9) as a function of  $b$  for 2D frictionless, elastic disks.  $\Theta_c^l$  is independent of  $b$  for  $b \geq 5$ , when the fluid force in the bulk is weak.  $\Theta_0^h$  is nearly independent of  $b$  for all  $b$ .  $\Theta_c^h$  is particularly sensitive to changes in the fluid profile, yielding hysteresis that increases with a stronger fluid flow above the bed. The hysteresis disappears when grain-grain dissipation is included or a quadratic drag law is used, which causes  $\Theta_c^h \rightarrow \Theta_0^h$ .

correspond to  $n$ -mers with  $n = 2$  (diamonds), 3 (triangles), 4 (squares), and 5 (stars). Both  $\Theta_c^l$  and  $\Theta_c^h$  increase by less than 50% with increasing friction, which is still comparable to the scatter in the experimental and field data shown in Fig. 1.

### C. Onset of grain motion

Thus far, we have argued that grain dynamics at varying  $\text{Re}_*$  play a dominant role in determining  $\Theta_c(\text{Re}_*)$ , as opposed to static force and torque balance of individual grains in typical pocket geometries. However, in simulations as well as natural or experimental systems, the initial onset of grain motion must follow from a breakdown of force and torque balance on one or more grains. In this section, we show data for the initiation of sustained grain motion, which, in the limit of large systems, always occurs at the same dynamical boundary  $\Theta_c(\text{Re}_*)$  that denotes the minimum applied fluid stress at which mobilized systems are able to stop. As the system size is increased in our model, it becomes increasingly likely to find an unstable grain, which will initiate permanent motion. We show that local motion in one of many uncorrelated subsystems leads to global sustained grain motion using Weibullian weakest-link statistics [65, 66]. Additionally, we find that the characteristic time  $t_m$  for the bed to fully mobilize diverges at  $\Theta_c$ , consistent with a dynamical instability at  $\Theta = \Theta_c$  that is activated by a single mobilized region.

If we consider the bed to be a composite system of  $M$  *uncorrelated* subsystems that begin to move if any of the subsystems move at  $\Theta > \Theta_c$  (when grain motion will be sustained indefinitely), then the cumulative distribution  $C_M(\Theta)$  for the initiation of grain motion in the collective system is related to that of a single subsystem  $C(\Theta)$  by

$$1 - C_M(\Theta) = [1 - C(\Theta)]^M. \quad (11)$$

By assuming a Weibull distribution for  $C(\Theta)$  [65–67]

$$C(\Theta) = 1 - \exp \left[ - \left( \frac{\Theta - \Theta_c}{\beta} \right)^\alpha \right], \quad (12)$$



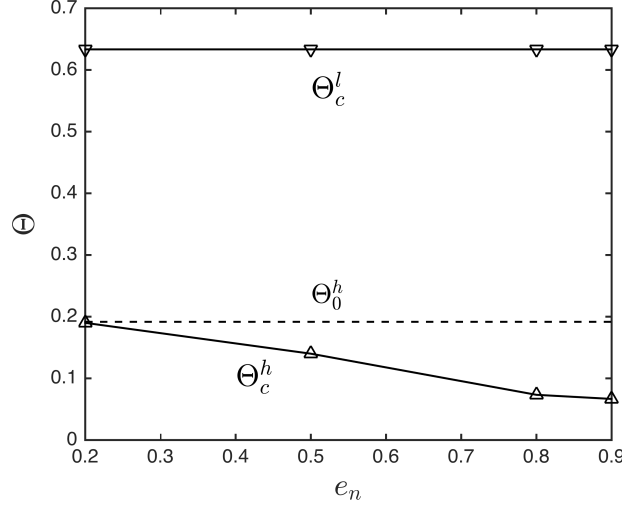


FIG. 13. The plateau values for frictionless disks as a function of  $e_n$ , with  $b = 5$ .  $\Theta_c^l$  is independent of  $e_n$ , and  $\Theta_c^h$  approaches the minimum value of  $\Theta$  to initiate grain motion for  $\text{Re}_* \gg 1$  as  $e_n \rightarrow 0$ .

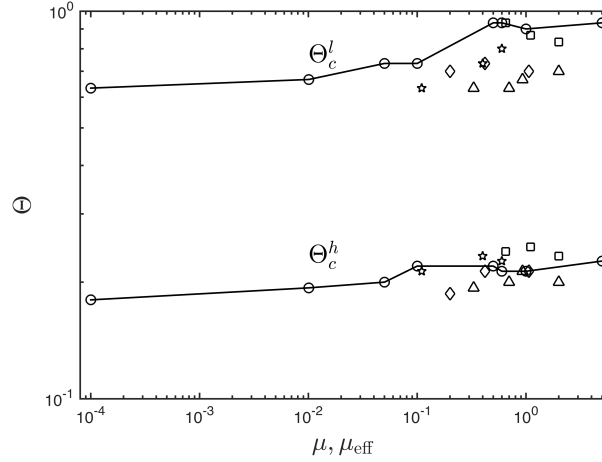


FIG. 14. The plateau values  $\Theta_c^l$  and  $\Theta_c^h = \Theta_0^h$  (for quadratic drag or small  $e_n$ ) are plotted as a function of friction coefficient  $\mu$  or  $\mu_{\text{eff}}$ . Solid lines with open circles show data for disks with Cundall-Strack friction. Other open symbols correspond to grain clusters with  $n = 2$  (diamonds), 3 (triangles), 4 (squares), and 5 (stars). The agreement between the grain-asperity model and the Cundall-Strack friction model is generally better as  $n$  increases.

then  $C_M(\Theta)$  in Eq. (11) has the same form with  $\alpha_M = \alpha$  and  $\beta_M = \beta M^{-1/\alpha}$ . As in our previous study [47], we find that this scaling holds for all systems we have considered here. This means that Eq. (11) applies, confirming that global grain motion is initiated by a single member of a collection of uncorrelated subsystems (i.e., local pockets). In the limit of large system size, we find that grain motion is always initiated at  $\Theta_c$ .

For a given system with static grains, we slowly increase  $\Theta$  until sustained grain motion occurs at  $\Theta = \Theta_f > \Theta_c$ . Figure 15 shows the distributions of the excess stress  $\Theta_f - \Theta_c$  required to initiate sustained grain motion in ensembles of static 3D systems as  $\Theta$  is slowly increased, computed with a quadratic drag law. These ensembles are prepared at  $\Theta \approx 0.067 < \Theta_c$  with a fill height of  $5D$  and a cross stream width of  $4D$ , and we vary the stream-wise distance  $W/D$  between 2.5 and 40. These distributions collapse when rescaled by their mean, as shown in the inset, with a shape parameter  $\alpha \approx 2.2$ . (This value is comparable to that measured in the frictionless, elastic case, where we found  $\alpha \approx 2.6$  [47].) The scaling of mean excess stress  $\Theta_f - \Theta_c$  is consistent with a power law scaling with exponent  $-1/\alpha$ , confirming Eqs. (11) and (12). For systems that fail, we measure the mobilization time  $t_m$ , which we define as the time required for the grain flux  $q$  to go from zero to the steady-state value. This quantity is plotted versus  $\Theta$  in Fig. 15, and it diverges at  $\Theta_c$ , like the divergence of  $t_s$  shown in Fig. 11.

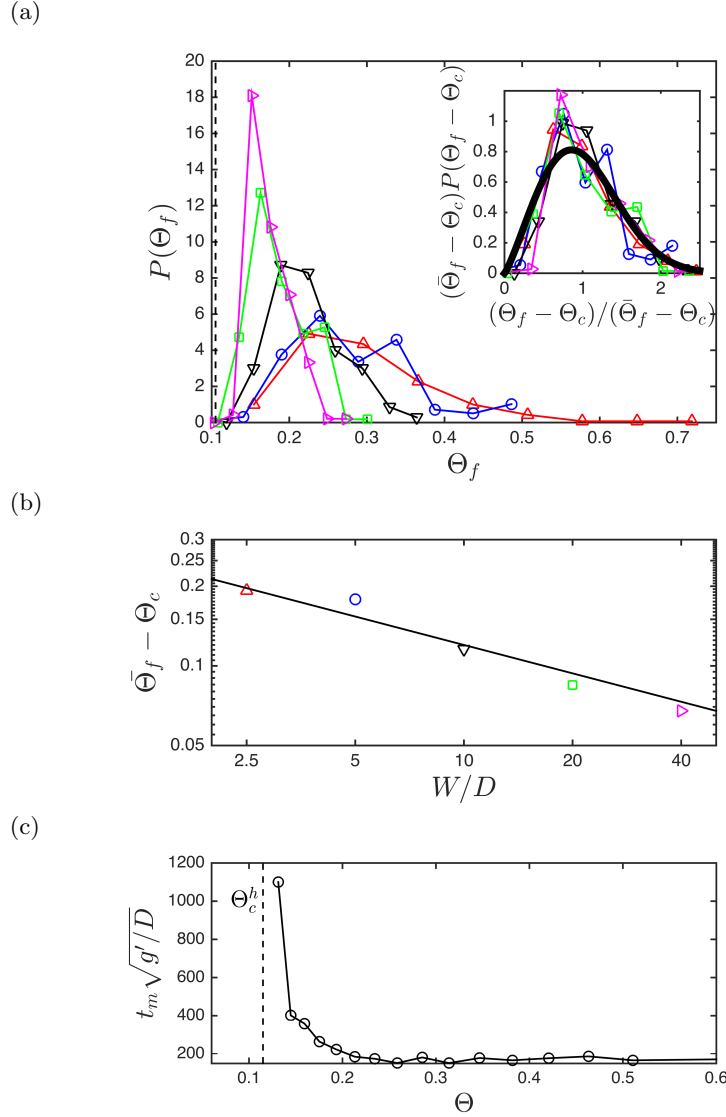


FIG. 15. (a) The probability distributions  $P(\Theta_f)$  of the Shields number  $\Theta_f$  required to initiate sustained grain motion in an initially static 3D system as  $\Theta$  is slowly increased, computed with a quadratic drag law. These ensembles were prepared with  $\Theta = 0.033 < \Theta_c$ ,  $\text{Re}_* \approx 100$  ( $\text{Re}_p = 3000$ ) and  $e_n = 0.5$ . Each simulation has a fill height  $5D$ , a cross-stream width of  $4D$ , and a stream-wise distance  $W/D$ , which we vary between 2.5 and 40. The inset shows that these distributions collapse when rescaled by  $\bar{\Theta}_f - \Theta_0$ , and the thick black line shows a Weibull distribution with shape parameter  $\alpha = 2.2$ . (b) The mean excess stress  $\bar{\Theta}_f - \Theta_0$  for the initiation of sustained grain motion decreases as a power law with exponent  $-1/\alpha$ , in accordance with Eqs. (11) and (12). (c) The mean normalized mobilization time  $t_m \sqrt{g'/D}$ , binned and averaged over  $\Theta$ .  $t_m$  is defined as the time required for the grain flux  $q$  to rise from zero to the steady-state value.

Figure 16 shows the same data, but for 2D systems using frictional grains, both with Cundall-Strack friction and the grain-asperity model. We again observe a good agreement with Eqs. (11) and (12) with  $\alpha \approx 2.4$ . We note that the primary difference between the frictionless case [47] and the frictional results shown here is in the effective system size  $M_{\text{eff}} = W_{\text{eff}} H_{\text{eff}}$ . In systems with tangential forces, where  $W$  is larger than a few grains, we find that  $M_{\text{eff}} = W$ , and the system height is nearly irrelevant. For frictionless disks,  $H_{\text{eff}}$  is calculated by integrating the probability of the initiation of grain motion over the depth of the system, which is equal to the fluid force profile. Thus, friction strongly suppresses the initiation of surface grain motion from rearrangements below the surface. The open star symbols in Fig. 16 show the statistics for  $\Theta_f$  for ensembles of 5-mers with  $\mu_{\text{eff}} = 0.6$  that were allowed to settle at  $\Theta = 0.033$  and  $\text{Re}_* \approx 10$  ( $\Gamma = 0.02$ ) for width  $W/D = 5, 10, 20$ , and 40, and depth  $ND/W = 10, 20$ , and 40. These 5-mers have  $\mu_{\text{eff}} \approx 0.6$ , which sufficiently suppresses grain rearrangements deep in the bed such that the collapse is good for  $M_{\text{eff}} = W$ .

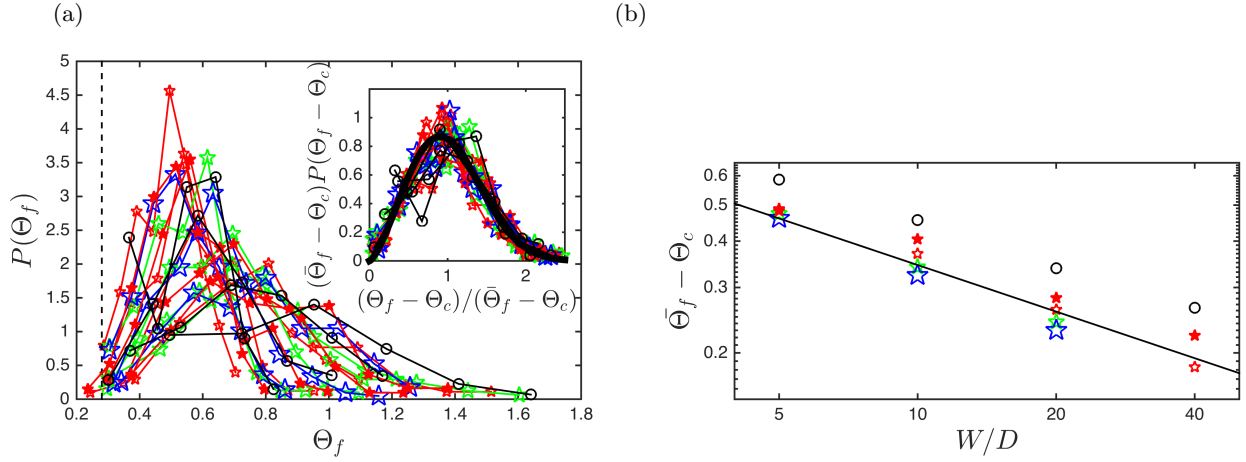


FIG. 16. (a) The probability distributions  $P(\Theta_f)$  of the Shields number  $\Theta_f$  where sustained grain motion is initiated ensembles of 2D, frictional, static systems, computed with a linear drag law. All ensembles shown here are prepared with  $\text{Re}_* \approx 10$  ( $\Gamma = 0.02$ ) and  $e_n = 0.8$ . Open symbols correspond to systems settled at  $\Theta = 0.033$ : disks with Cundall-Strack friction with  $\mu = 0.6$  and fill height  $10D$  (open black circles), as well as grain clusters (5-mers with  $\mu_{\text{eff}} = 0.6$ ) with fill heights of  $10D$  (open red stars),  $20D$  (open green stars), and  $40D$  (open blue stars), where the size of these symbols increases with fill height. The inset shows that these distributions collapse when rescaled by  $\bar{\Theta}_f - \Theta_c$ , and the thick black line shows a Weibull distribution with shape parameter  $\alpha = 2.4$ . (b) The mean excess stress for the initiation of grain motion  $\bar{\Theta}_f - \Theta_c$  decreases as a power law with exponent  $-1/\alpha$ , in accordance with the behavior of Eqs. (11) and (12). Open stars lie nearly on top of each other, despite large variation in depth; this illustrates that tangential forces greatly suppress rearrangements in the bed that lead to grain motion (see text for discussion). Filled stars, which settled at  $\Theta = 0.067$  instead of  $\Theta = 0.033$ , also show the mean excess stress decreases according to a power law with exponent  $-1/\alpha$ , but with larger magnitude. This means that systems that settle at a larger  $\Theta$  will fail at greater  $\Theta_f$ , an effect that we do not observe in frictionless systems. Disks with Cundall-Strack friction show the same scaling as grain clusters, but with larger  $\bar{\Theta}_f - \Theta_c$ .

We also note that the initiation of grain motion in systems with tangential forces depends on preparation history in a way that is different from frictionless systems. Specifically, systems with tangential contact forces that settle at a larger value of  $\Theta$  tend to fail at larger values of  $\Theta_f$ . In frictionless simulations, we found no variation of the statistics of  $\Theta_f$  with the value of  $\Theta$  at which the system settled. The open stars shown in Fig. 16 settled at  $\Theta = 0.033$ , whereas the filled red stars settled at  $\Theta = 0.067$ . Settling at a larger value of  $\Theta$  makes these systems statistically stronger on average but does not affect  $\Theta_c$ .

## V. DISCUSSION

In this manuscript, we introduced a physical mechanism for how  $\text{Re}_*$ -dependent grain dynamics can affect the critical applied fluid stress  $\Theta_c$  required to sustain permanent grain motion. Using numerical simulations, we showed that the minimum dimensionless shear force to maintain grain motion can be described by a function  $\Theta_c(\text{Re}_*)$  that consists of two distinct regimes. At  $\text{Re}_* < 1$ , grain dynamics are viscous dominated, and grains are not significantly accelerated between interactions with the bed. This means that grains are unlikely to bounce over a stable surface configuration or disrupt existing pockets during interactions with surface grains. In this regime, more geometrical configurations are available to grains as they search for stability, and grains find a state that is stable to a maximum Shields number of  $\Theta_c^l \approx 0.28$ . At  $\text{Re}_* > 10$ , grains are accelerated significantly between interactions with the bed. Based on the physical reasoning given in Section II, this makes some geometrical configurations inaccessible to the grains. This picture is confirmed by our numerical results, where grains that are sheared by the exact same fluid flow at  $\text{Re}_* > 10$  are unable to find these configurations that are stable in the region  $\Theta_c^h < \Theta < \Theta_c^l$ , where  $\Theta_c^h \approx 0.11$ . In addition, if we approximate lift forces from Wiberg and Smith [29], our results are quantitatively consistent with the Shields curve over the full range of  $\text{Re}_*$ .

These results suggest that the most common physical picture of the onset of sediment transport, namely the conditions at which static equilibrium is violated for surface grains, should be updated to include grain reorganization dynamics. The divergence of the transition times  $t_s$  and  $t_m$  at  $\Theta = \Theta_c$  suggest the existence of a dynamical instability. Theories that account for when mobile grains can stop may be more successful than simply focusing on when static grains can first move. The roughness and geometry of the granular bed must play a role, but its role should be

expanded from a focus on pocket angles of surface grains to a broader picture that describes the dynamics of grains as they traverse a rough, granular bed. In our theoretical analysis, we include this effect by assuming that grains will collide with the bed after moving roughly one grain diameter. This picture is supported by the data shown in Fig. 8.

Our results also suggest that previous approaches, which analyzed a single representative pocket geometry of a surface grain, could possibly be improved by accounting for the distribution of pocket geometries. Such an approach is similar in spirit to the results presented in Section IV C, where for large systems we find that grain motion will always be initiated somewhere in the system once  $\Theta$  exceeds  $\Theta_c$ . We argue that the grain dynamics that follow the initial force imbalance are important. Unsteadiness in the fluid flow, from turbulence or other external sources of fluctuations, can initiate grain motion, which will then be sustained only above the dynamical boundary  $\Theta_c$ . Our simulations do not include any explicit temporal fluctuations, and there are likely important differences that arise when turbulence or other unsteadiness in the fluid stress is included, such as intermittency and large fluctuations in the grain dynamics near  $\Theta_c$  [68].

Finally, the boundaries  $\Theta_c(\text{Re}_*)$  for simulations with linear and quadratic drag laws show striking agreement. At  $\text{Re}_* \ll 1$ , these two approaches are expected to agree, since Stokes drag dominates in both cases. However, at  $\text{Re}_* \gg 1$ , such good agreement is quite surprising. This means that, with regard to how grains search for stable configurations to an applied shear force, the form of the drag law is not important. The only relevant parameters are the shear stress  $\Theta$ , the bed collision time  $\tau_\Theta$ , and the characteristic time for a grain to equilibrate to the flow, which is given either by  $\tau_\nu$  or  $\tau_I$ . For  $\text{Re}_* \gg 1$ , the fluid equilibration time scales are always longer than the bed collision time scale. Thus, the minimum value of  $\Theta$  to initiate sustained grain motion from a static bed is the same for both drag laws. For a linear drag law, we note that large restitution coefficients cause grains to bounce up into the fluid flow and accelerate in a way that is physically unreasonable in subaqueous sediment transport. This is the cause of the hysteresis shown in Fig. 9. When  $e_n$  is decreased, these effects are suppressed and the hysteresis vanishes. For linear drag with small  $e_n$  and quadratic drag for all  $e_n$ , the onset and cessation of grain motion occur at the same boundary, since the dominant physics relates to surface grain dynamics. However, we note that for the case of Aeolian sediment transport, the sediment grains are much denser than air,  $\rho_g/\rho_f \sim 2000$ , which yields  $\tau_I/\tau_\Theta \sim 40 - 50$ . This means saltating grains are substantially accelerated, and grain-grain collisions can be relatively elastic upon collision with the bed. Under these conditions, our results predict hysteresis, where motion is sustained by fast moving grains colliding with the bed [43, 69] as in our simulations with a linear drag law and large  $e_n$ .

Future work will focus on microstructural differences between contact geometries in the different regimes of  $\text{Re}_*$ . Our results show that grains at  $\text{Re}_* > 10$  are unable to find configurations that are stable to an identical applied shear force profile at  $\text{Re}_* < 1$ . Understanding the structure of these grain configurations may clarify why they are inaccessible at high  $\text{Re}_*$ .

## ACKNOWLEDGMENTS

This work was supported by the US Army Research Office under Grant No. W911NF-14-1-0005 (A.H.C., N.T.O., C.S.O.) and by the National Science Foundation (NSF) Grant No. CBET-0968013 (M.D.S.). This work also benefited from the facilities and staff of the Yale University Faculty of Arts and Sciences High Performance Computing Center and the NSF (Grant No. CNS-0821132) that, in part, funded acquisition of the computational facilities. We thank Arshad Kudrolli for his help in understanding various aspects of this problem, and we thank Michael Loewenberg for helpful discussions. To access the simulation results shown here, please contact A.H.C. at [abram.clark@yale.edu](mailto:abram.clark@yale.edu).

- 
- [1] Walter G Knisel *et al.*, “Creams: A field-scale model for chemicals, runoff and erosion from agricultural management systems.” USDA Conservation Research Report (1980).
  - [2] D.E. Walling, “The sediment delivery problem,” *Journal of Hydrology* **65**, 209 – 237 (1983).
  - [3] Kenneth G Renard, GR Foster, GA Weesies, DK McCool, DC Yoder, *et al.*, *Predicting soil erosion by water: A guide to conservation planning with the Revised Universal Soil Loss Equation (RUSLE)*, Vol. 703 (United States Department of Agriculture Washington, DC, 1997).
  - [4] Subhasish Dey, “Fluvial hydrodynamics: Hydrodynamic and sediment transport phenomena,” (Springer Berlin Heidelberg, Berlin, Heidelberg, 2014) Chap. Sediment Threshold, pp. 189–259.
  - [5] J. M. Buffington and D. R. Montgomery, “A systematic analysis of eight decades of incipient motion studies, with special reference to gravel-bedded rivers,” *Water Resources Research* **33**, 1993–2029 (1997).
  - [6] Ning Xu and Corey S. O’Hern, “Measurements of the yield stress in frictionless granular systems,” *Phys. Rev. E* **73**, 061303 (2006).
  - [7] P. J. Barrett, “The shape of rock particles, a critical review,” *Sedimentology* **27**, 291–303 (1980).

- [8] S. A. Schumm, "The shape of alluvial channels in relation to sediment type," U.S. Geol. Surv. Prof. Pap. **352B**, 17–30 (1960).
- [9] Gary Parker, "Hydraulic geometry of active gravel rivers," Journal of the Hydraulics Division **105**, 1185–1201 (1979).
- [10] Donald A Nield and Adrian Bejan, *Mechanics of Fluid Flow Through a Porous Medium* (Springer, 2013).
- [11] Grove Karl Gilbert and Edward Charles Murphy, *The transportation of debris by running water*, 86 (US Government Printing Office, 1914).
- [12] H.J. Casey, *Über die geschiebbewegung*, Ph.D. thesis, Teknikal Hochschule-Scharlottenburg, Berlin, Germany (1935).
- [13] A. Shields, "Anwendung der ähnlichkeitsmechanik und der Turbulenzforschung auf die Geschiebbewegung," in *Mitteilungen der Preussischen Versuchsanstalt für Wasserbau und Schiffbau*, Vol. 26 (1936).
- [14] USWES, "Flume tests made to develop a synthetic sand which will not form ripples when used in movable bed models," Tech. Memo. 99-1, United States Waterways Experiment Station, Vicksburg, Mississippi (1936).
- [15] C. M. White, "The equilibrium of grains on the bed of a stream," Proc.R.Soc.London, Ser.A **174**, 322–338 (1940).
- [16] V. A. Vanoni, Transportation by Water Suspension, ASCE **3**, 67 (1946).
- [17] Eugen Meyer-Peter and R Müller, "Formulas for bed-load transport," (IAHR, 1948).
- [18] C.R. Neill, "Mean velocity criterion for scour of coarse uniform bed material," (IAHR, 1967).
- [19] A. J. Grass, "Initial instability of fine bed sand," Journal of Fluid Mechanics **50**, 619 (1970).
- [20] S. J. White, "Plane bed thresholds of fine grained sediments," Nature **228**, 152–153 (1970).
- [21] E. Karahan, *Initiation of motion for uniform and nonuniform materials*, Ph.D. thesis, Technical University, Istanbul, Turkey, (1975).
- [22] P. A. Mantz, "Incipient transport of fine grains and flakes by fluids – extended Shields diagram," Journal of the hydraulics division **103**, 601–615 (1977).
- [23] Mehmet Selim Yalin and Emin Karahan, "Inception of sediment transport," Journal of the hydraulics division **105**, 1433–1443 (1979).
- [24] M. C. Miller, I. N. McCave, and P. D. Komar, "Threshold of sediment motion under unidirectional currents," Sedimentology **24**, 507–527 (1977).
- [25] M.S. Yalin, *Mechanics of sediment transport* (Pergamon Press, 1972).
- [26] Leo C Van Rijn, *Principles of sediment transport in rivers, estuaries and coastal seas*, Vol. 1006 (Aqua publications Amsterdam, 1993).
- [27] D Paphitis, "Sediment movement under unidirectional flows: an assessment of empirical threshold curves," Coastal Engineering **43**, 227 – 245 (2001).
- [28] Yuichi Iwagaki, "Hydrodynamical study on critical tractive force," Transaction of the Japanese Society of Civil Engineers **41**, 1–21 (1956).
- [29] Patricia L. Wiberg and J. Dungan Smith, "Calculations of the critical shear stress for motion of uniform and heterogeneous sediments," Water Resources Research **23**, 1471–1480 (1987).
- [30] Chi-Hai Ling, "Criteria for incipient motion of spherical sediment particles," Journal of Hydraulic Engineering **121**, 472–478 (1995).
- [31] Subhasish Dey, "Sediment threshold," Applied Mathematical Modelling **23**, 399 – 417 (1999).
- [32] Subhasish Dey and Koustuv Debnath, "Influence of streamwise bed slope on sediment threshold under stream flow," Journal of irrigation and drainage engineering **126**, 255–263 (2000).
- [33] James W Kirchner, William E Dietrich, Fujiko Iseya, and Hiroshi Ikeda, "The variability of critical shear stress, friction angle, and grain protrusion in water-worked sediments," Sedimentology **37**, 647–672 (1990).
- [34] ED Andrews, "Marginal bed load transport in a gravel bed stream, sagehen creek, california," Water Resources Research **30**, 2241–2250 (1994).
- [35] John M Buffington, William E Dietrich, and James W Kirchner, "Friction angle measurements on a naturally formed gravel streambed: Implications for critical boundary shear stress," Water Resources Research **28**, 411–425 (1992).
- [36] Michael P Lamb, William E Dietrich, and Jeremy G Venditti, "Is the critical shields stress for incipient sediment motion dependent on channel-bed slope?" Journal of Geophysical Research: Earth Surface **113** (2008).
- [37] H. Reichardt, "Vollständige darstellung der turbulenten geschwindigkeitsverteilung in glatten leitungen," ZAMM - Zeitschrift für Angewandte Mathematik und Mechanik **31**, 208–219 (1951).
- [38] Herrmann Schlichting and Klaus Gersten, *Boundary-layer theory* (Springer Science & Business Media, 2003).
- [39] François Charru, Hélène Mouilleron, and Olivier Eiff, "Erosion and deposition of particles on a bed sheared by a viscous flow," Journal of Fluid Mechanics **519**, 55–80 (2004).
- [40] Alexander E Lobkovsky, Ashish V Orpe, Ryan Molloy, Arshad Kudrolli, and Daniel H Rothman, "Erosion of a granular bed driven by laminar fluid flow," Journal of Fluid Mechanics **605**, 47–58 (2008).
- [41] A. Hong, M. Tao, and A. Kudrolli, "Onset of erosion of a granular bed in a channel driven by fluid flow," Phys. Fluids **27**, 013301 (2015).
- [42] Mark W Schmeeckle and Jonathan M Nelson, "Direct numerical simulation of bedload transport using a local, dynamic boundary condition," Sedimentology **50**, 279–301 (2003).
- [43] M. V. Carneiro, T. Pähz, and H. J. Herrmann, "Jump at the onset of saltation," Phys. Rev. Lett. **107**, 098001 (2011).
- [44] Orenco Durán, Bruno Andreotti, and Philippe Claudin, "Numerical simulation of turbulent sediment transport, from bed load to saltation," Physics of Fluids **24**, 103306 (2012).
- [45] J. Capecelatro and O. Desjardins, "Eulerian-Lagrangian modeling of turbulent liquid-solid slurries in horizontal pipes," Intl. J. Multiphase Flow **55**, 64–79 (2013).

- [46] M Nabi, de HJ Vriend, E Mosselman, CJ Sloff, and Y Shimizu, “Detailed simulation of morphodynamics: 2. Sediment pickup, transport, and deposition,” *Water Resources Research* **49**, 4775–4791 (2013).
- [47] Abram H. Clark, Mark D. Shattuck, Nicholas T. Ouellette, and Corey S. O’Hern, “Onset and cessation of motion in hydrodynamically sheared granular beds,” *Phys. Rev. E* **92**, 042202 (2015).
- [48] Marco Pilotti and Giovanni Menduni, “Beginning of sediment transport of incoherent grains in shallow shear flows,” *Journal of Hydraulic Research* **39**, 115–124 (2001).
- [49] S. K. Robinson, “Coherent motions in the turbulent boundary layer,” *Annu. Rev. Fluid Mech.* **23**, 601–639 (1991).
- [50] P. Diplas, C. L. Dancey, A. O. Celik, M. Valyrakis, K. Greer, and T. Akar, “The role of impulse on the initiation of particle movement under turbulent flow conditions,” *Science* **322**, 717–720 (2008).
- [51] R. J. Hardy, J. L. Best, S. N. Lane, and P. E. Carbonneau, “Coherent flow structures in a depth-limited flow over a gravel surface: The role of near-bed turbulence and influence of Reynolds number,” *J. Geophys. Res.* **114**, F01003 (2009).
- [52] Mark W Schmeckle, “Numerical simulation of turbulence and sediment transport of medium sand,” *Journal of Geophysical Research: Earth Surface* **119**, 1240–1262 (2014).
- [53] John C Roseberry, Mark W Schmeckle, and David Jon Furbish, “A probabilistic description of the bed load sediment flux: 2. particle activity and motions,” *Journal of Geophysical Research: Earth Surface* **117** (2012).
- [54] Donna N. Perera and Peter Harrowell, “Stability and structure of a supercooled liquid mixture in two dimensions,” *Phys. Rev. E* **59**, 5721–5743 (1999).
- [55] Robin J Speedy, “Glass transition in hard disc mixtures,” *The Journal of Chemical Physics* **110**, 4559–4565 (1999).
- [56] Kai Zhang, W. Wendell Smith, Minglei Wang, Yanhui Liu, Jan Schroers, Mark D. Shattuck, and Corey S. O’Hern, “Connection between the packing efficiency of binary hard spheres and the glass-forming ability of bulk metallic glasses,” *Phys. Rev. E* **90**, 032311 (2014).
- [57] P. A. Cundall and O. D. L. Strack, “A discrete numerical model for granular assemblies,” *Géotechnique* **29**, 47–65 (1979).
- [58] J. Schäfer, S. Dippel, and D. E. Wolf, “Force schemes in simulations of granular materials,” *J. Phys. I France* **6**, 5 (1996).
- [59] F.-L. Yang and M. L. Hunt, “Dynamics of particle-particle collisions in a viscous liquid,” *Physics of Fluids* **18**, 121506 (2006).
- [60] G. G. Joseph, R. Zenit, M. L. Hunt, and A. M. Rosenwinkel, “Particlewall collisions in a viscous fluid,” *Journal of Fluid Mechanics* **433**, 329–346 (2001).
- [61] Mark W Schmeckle, Jonathan M Nelson, John Pitlick, and James P Bennett, “Interparticle collision of natural sediment grains in water,” *Water Resources Research* **37**, 2377–2391 (2001).
- [62] Volkhard Buchholtz and Thorsten Pöschel, “Numerical investigations of the evolution of sandpiles,” *Physica A: Statistical Mechanics and its Applications* **202**, 390 – 401 (1994).
- [63] Stefanos Papanikolaou, Corey S. O’Hern, and Mark D. Shattuck, “Isostaticity at frictional jamming,” *Phys. Rev. Lett.* **110**, 198002 (2013).
- [64] Guo-Jie Gao, Jerzy Bławdziewicz, and Corey S. O’Hern, “Frequency distribution of mechanically stable disk packings,” *Phys. Rev. E* **74**, 061304 (2006).
- [65] W. Weibull, *A Statistical Theory of the Strength of Materials*, Ingeniörsvetenskapsakademiens handlingar (Generalstabens litografiska anstalts förlag, 1939).
- [66] W. Weibull, “A statistical distribution function of wide applicability,” *J. Appl. Mech.* **18**, 293–297 (1951).
- [67] Scott V. Franklin, “Extensional rheology of entangled granular materials,” *EPL (Europhysics Letters)* **106**, 58004 (2014).
- [68] Christian González, David H. Richter, Diogo Bolster, Samuel Bateman, Joseph Calantoni, and Cristián Escarriaza, “Characterization of bedload intermittency near the threshold of motion using a lagrangian sediment transport model,” *Environmental Fluid Mechanics*, 1–27 (2016).
- [69] S Mitha, MQ Tran, BT Werner, and PK Haff, “The grain-bed impact process in aeolian saltation,” *Acta Mechanica* **63**, 267–278 (1986).